Image Processing for Synthetic Aperture Radar System on Light-weight Drone

Senior Honors Thesis

Presented in Partial Fulfillment of the Requirements for Graduation with Distinction in the College of Engineering of The Ohio State University

By

Shiqi Yang

Department of Electrical and Computer Engineering

Advisor:

Professor Lee Potter

Department of Electrical and Computer Engineering

Abstract

This project focuses on the implementation of image processing software for a drone-based synthetic aperture radar (SAR) system. The drone-SAR system is under development by a student design team. The specific contributions in this thesis are two stages of software development. In the first part, to achieve a basic image formation function, we implemented and demonstrated backprojection imaging using radar data and global positioning system (GPS) data collected by the team. In the second part, we researched and implemented an autofocus algorithm, in order to generate high-resolution images in the inevitable presence of measurement errors greater than one-quarter wavelength.

Acknowledgements

The author would like to thank his drone-SAR project team, which includes David Giffin, Sarah Greenbaum, Joy Smith, Brandi Downs, Arron Pycraft, Luke Smith, Daniel Wharton and Jingong Huang, who supported the author for the completion of this thesis project. The author would also like to thank Professor Potter for his mentoring and helpful advice, which ensured the successful completion of this thesis project and this thesis.

Table of Contents

List of Tables

List of Figures

CHAPTER 1: Introduction

1.1 Goals

A synthetic aperture radar (SAR) system is capable of providing vision under special circumstances when optical systems may fail: at night, through clouds, though fog, through dust and etc [1]. In autumn of 2017, a SAR project team in the department of Electrical and Computer Engineering at The Ohio State University (OSU) built a C-band SAR system on a rail. The system could generate images of reflectivity at a range of 7 meters [2]. Based on previous work in autumn 2017, a new SAR project team was formed in spring of 2018, aiming at making an X-band SAR system on a small drone. The new X-band SAR system needs to have a minimum detectable range of 80 meters and it must generate a 100×100 pixel image with a resolution less than one meter. The cost of the system should not exceed $10,000 and the weight of the system is kept on the order of few kilograms [3].

1.2 Teamwork

The drone-SAR project team is divided into four groups. People in the first group focus on system integration and drone operation; the second group is responsible for GPS test and data collection; people in the third group focus on X-band radar evaluation and radar data collection; the main task for people in the last group is software development for image processing in the system. Table 1 shows the team division. The team carried out project management through Google Drive and GitHub. During the project cycle, weekly meetings were hold to report the progress.

Table 1: Drone-SAR Project Team Division

Focus Area	Members
System Integration & Drone Operation	David Giffin, Sarah Greenbaum, Joy Smith
GPS Test & GPS Data Integration	Brandi Downs
X-band Automotive Radar Evaluation & Radar Data Collection	Aaron Pycraft, Luke Smith, Daniel Wharton
Image Processing	Jingong Huang, Shiqi Yang

1.3 Standards and Regulations

In this project, the drone-SAR system must satisfy regulations from the Federal Aviation Administration (FAA) [4], the Federal Communications Commission (FCC) [5] and OSU [6]. Table 2 [3] shows detailed information about constraints from different regulations to the drone-SAR project. In order to satisfy FAA, FCC and OSU regulations, the team made a series of decisions, which were also included in Table 2.

Table 2: Regulations and Team Decisions

Components	Application	Regulations	Regulation Limit	Decisions for Compliance
Drone	Flight Attitude	14 CFR Part 107 from FAA	< 400 feet	Fly Under 400 feet
Drone	Weight	14 CFR Part 107 from FAA	< 55 lbs	Estimated weight is << 55 lbs
Drone	Drone Operation	14 CFR Part 107 from FAA	Require a remote pilot airman certificate	One member in the team needs to pass the through an FAA-approved administration site.
Drone	Drone Operation	Use of Unmanned Aircraft System from OSU	Require an Export Review prior to drone operation	The team filled an Export Review Request Form and received permission to fly the drone
X-band Radar	Bandwidth	47 CFR §15.521 from FCC	< 500 MHz	Keep operational bandwidth under 500 MHz
X-band Radar	Restricted Frequency Bands of Operation	47 CFR §15.205 from FCC	9.3 – 9.5 GHz or 10.6 – 12.7 GHz	Operate the radar with a bandwidth of 400 MHz and a center frequency of 9.8 GHz

1.4 Specific Contribution

This report focuses on image processing for the drone-SAR system. The goal is to compute 2-D high-resolution images as the output of the system based on information from other modules. In the first stage, we implement the backprojection algorithm [7] to achieve a fundamental image formation function in the drone-SAR system.

In reality, SAR images would be smeared or blurred because of non-ideal factors, such as motion measurement errors, noises, unstable behaviors of the radar system, etc. In order to form high-quality images from drone-SAR system without extra hardware cost, application of autofocus algorithm is necessary. In the second stage, a time-domain autofocus is integrated into the software [8].

1.5 Outline of Thesis

In Chapter 2 of this report, we performed analysis to operating principles of the X-band radar in and introduced backprojection algorithm for image construction. In Chapter 3, we presented a time-domain autofocus algorithm to enhance the quality of SAR image. We demonstrated the project results in Chapter 4 and carried out result analysis in Chapter 5. In Chapter 6, we showed conclusions from this project and provided suggestions to future works.

CHAPTER 2: Backprojection Algorithm

2.1 FMCW & Stretch Processing

2.1.1 Signal Model

Frequency modulation continuous wave (FMCW) is a common technique applied in radar systems. Stretch processing [9] is a signal processing algorithm for a FMCW radar system. A general FMCW radar model is shown in Figure 1.

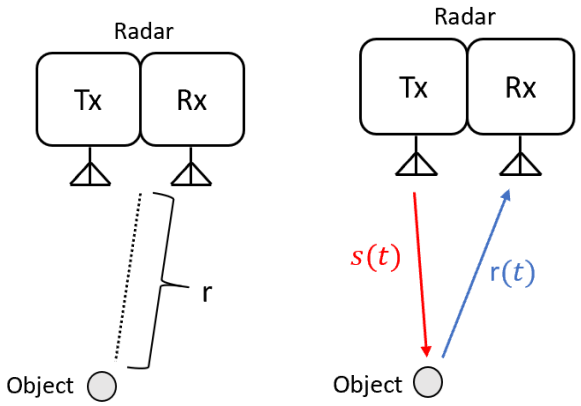

Figure 1: FMCW Radar Model

Tx and Rx represent transmitter and receiver in FMCW radar system. As shown in Figure 1(a), the distance between radar and object is denoted as r. At the beginning of signal collection, the radar system sends out a transmission signal (also called a pulse), $s(t)$. When the transmission signal $s(t)$ hits the object, it gets reflected back to the radar system and caught by an antenna on receiver. The signal caught by the receiver is called received signal, and it is denoted as $r(t)$ in Figure 1(b). $s(t)$ and $r(t)$ are time-domain signals; variable t represents time.

In FMCW radar system, the transmission signal $s(t)$ is a linear frequency modulated (LFM) chirp wave:

$$s(t) = \cos((\omega_c + \alpha t) \cdot t), \quad -\frac{T}{2} \le t \le \frac{T}{2}. \qquad (1)$$

Several parameters are associated with the property of radar system:

ω_c	Carrier Frequency (rad/sec)
f_c	Carrier Frequency (Hz)
T	Sweep Time (s)
BW	Bandwidth (Hz)
α	Chirp Rate (rad/s^2)
c	Speed of propagation (m/s)

Relationships among these parameters are:

$$\omega_c = 2\pi f_c$$

$$\alpha = \frac{2\pi \cdot BW}{T}$$

The received signal $r(t)$ is a time-delayed and scaled version of $s(t)$. According to Figure 1(a), corresponding time delay associated with the distance, r, is:

$$t_{delay} = \frac{2r}{c} \text{ (unit: sec)}$$

where $2r$ means that the radar signal travels a distance of r to hit the object and travels another r to come back to receiver. $A(r)$ represents reflection signal at a distance r away from the radar[1] and it is called "range profile". In the ideal case, the received signal can be represented as follows[2]:

$$r(t) = A(r) \cdot s\left(t - t_{delay}\right) = A(r) \cdot s\left(t - \frac{2r}{c}\right)$$

$$r(t) = A(r) \cdot \cos\left(\omega_c\left(t - \frac{2r}{c}\right) + \alpha\left(t - \frac{2r}{c}\right)^2\right), \quad -\frac{T}{2} \le t \le \frac{T}{2} \qquad (2)$$

1. An image can be simply interpreted as a collection of pixels and each pixel has a certain value of strength. In this project, for image construction, the key is to find A(r).
2. The one-way propagation loss related to $\frac{1}{r^2}$ is ignored in the derivations of equations (2) and (3)

However, when nonideal factors are considered, they influence the received signal. At a distance r away from radar, we model the influences from nonideal factors by an attenuation $p(r)$ and a phase shift ϕ_r. As a result, the nonideal received signal under influences of noises can be expressed as:

$$r(t) = A(r) \cdot p(r) \cdot \cos\left(\omega_c\left(t - \frac{2r}{c}\right) + \alpha\left(t - \frac{2r}{c}\right)^2 + \phi_r\right), \quad -\frac{T}{2} \le t \le \frac{T}{2}. \qquad (3)$$

2.1.2 Stretch Processing

Discussions of stretch processing are based on equations (1) and (2). Frequency of transmission signal $s(t)$ is linearly changed with time; as a delayed version of $s(t)$, the received signal $r(t)$ is also an LFM signal and its frequency is also linearly changed with time. Figure 2(a) shows relationship between frequency and time for $s(t)$ and $r(t)$.

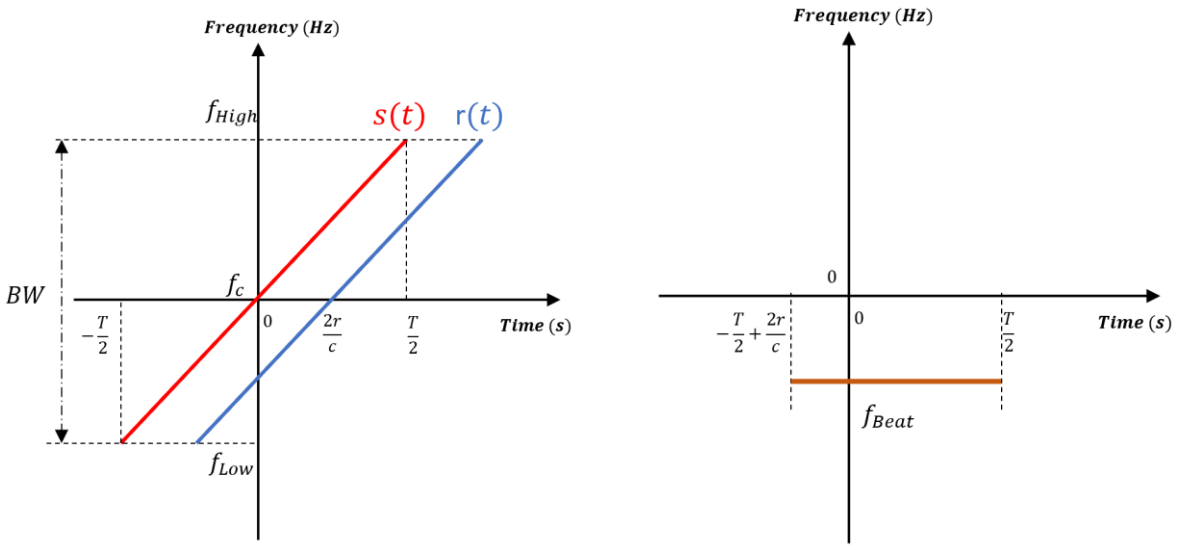

(a) (b)

Figure 2: FMCW Frequencies

(a) Frequency vs. Time for Transmission and Received Signal

(b) Beat Frequency

The instantaneous frequency of a cosine signal can be calculated by taking the derivative of its argument respect to time. Because signals $s(t)$ and $r(t)$ are cosine signals, their frequencies can be gained as follows:

$$f_{TX}(t) = \frac{d(\arg(s(t)))}{dt} = \frac{d((2\pi f_c + \alpha t)\cdot t)}{dt} = 2\pi f_c + 2\alpha t, \quad -\frac{T}{2} \le t \le \frac{T}{2} \qquad (4)$$

$$f_{RX}(t) = \frac{d(\arg(r(t)))}{dt} = \frac{d(2\pi f_c\left(t-\frac{2r}{c}\right)+\alpha\left(t-\frac{2r}{c}\right)^2)}{dt} = 2\pi f_c + 2\alpha(t-\frac{2r}{c}), \quad -\frac{T}{2} \le t \le \frac{T}{2} \qquad (5)$$

where $f_{TX}(t)$ is the frequency of transmission signal and $f_{RX}(t)$ is the frequency of received signal. Beat frequency is calculated by subtracting $f_{TX}(t)$ from $f_{RX}(t)$.

$$f_{Beat} = f_{RX}(t) - f_{TX}(t) = -\frac{4\alpha r}{c} \qquad (6)$$

Shown in equation (6), the beat frequency contains information about the distance between radar and object. By applying Fourier analysis to the signal containing beat frequency, we can extract information related to the distance between the radar and the object.

In this example, we consider a simple case with only one object in the field. Discussion shown above also applicable to more complex cases with multiple objects in the field. For instance, consider a case with N distinguishable objects in the field. When the radar transmission signal hits these N objects, each of them would generate its individual reflection to the transmission signal. The radar receiver would superimpose N reflection signals from N objects to construct the received signal. Then, the system would perform stretch processing on the received signal. By applying Fourier analysis to the output signal from stretch processing, we can identify the number of objects in the field, as well as their distances to the radar system.

2.1.3 Hardware Implementation of Stretch Processing

According to discussion in previous section, the key in stretch processing is frequency subtraction between the transmission and received signal. To implement the frequency subtraction, hardware architecture shown in Figure 3 is implemented in the radar receiver.

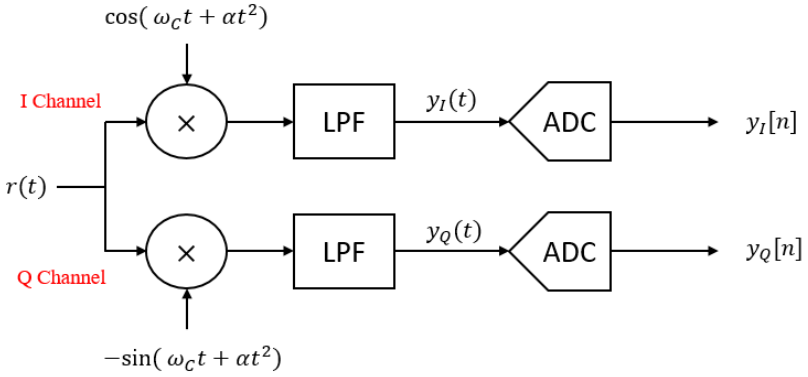

Figure 3: Radar Receiver Architecture

In the ideal case, according to equation (2), the received signal $r(t)$ is,

$$r(t) = A(r) \cdot \cos\left(\omega_c\left(t - \frac{2r}{c}\right) + \alpha\left(t - \frac{2r}{c}\right)^2\right), \quad -\frac{T}{2} \le t \le \frac{T}{2}$$

In I channel, when $r(t)$ is mixed with the transmission signal $s(t) = \cos(\omega_c t + \alpha t^2)$ and passed through the low-pass filter (LPF),

$$y_I(t) = LPF\{\ A(r) \cdot \cos\left(\omega_c\left(t - \frac{2r}{c}\right) + \alpha\left(t - \frac{2r}{c}\right)^2\right) \cdot \cos(\omega_c t + \alpha t^2)\ \}$$

$$y_I(t) = \frac{A(r)}{2} \cdot \cos\left(\frac{2r}{c}(\omega_c + 2\alpha t) - \frac{4\alpha r^2}{c^2}\right), \quad -\frac{T}{2} \le t \le \frac{T}{2} \qquad (7)$$

In Q channel, signal $-\sin(\omega_c t + \alpha t^2)$ can be gained by a 90° phase shift to $s(t)$. Similar to I channel, the output signal of the LPF can be expressed as:

$$y_Q(t) = -\frac{A(r)}{2} \cdot \sin\left(\frac{2r}{c}(\omega_c + 2\alpha t) - \frac{4\alpha r^2}{c^2}\right), \quad -\frac{T}{2} \le t \le \frac{T}{2} \qquad (8)$$

2.2 Backprojection Algorithm

2.2.1 Signal Model for Single Pulse

Based on signals $y_I(t)$ and $y_Q(t)$ in equations (7) and (8), signal $y(t)$, referred as "complex IQ data" can be constructed for post processing, as shown in equation (9). Complex IQ data, $y(t)$, contains information about beat frequency mentioned above.

$$y(t) = y_I(t) + j \cdot y_Q(t)$$

$$y(t) = \frac{A(r)}{2} \cdot e^{-j\frac{2r}{c}(\omega_c + 2\alpha t)} \cdot e^{j\left(\frac{4\alpha r^2}{c^2}\right)}, \quad -\frac{T}{2} \le t \le \frac{T}{2} \qquad (9)$$

In equation (9), c is the speed of light, α is the chirp rate of the radar system and r is the distance between radar and an object. Because $c^2 \gg 4\alpha r^2$, the exponential term $e^{j\left(\frac{4\alpha r^2}{c^2}\right)}$ can be ignored. Equation (9) can be simplified as:

$$y(t) = \frac{A(r)}{2} \cdot e^{-j\frac{2r}{c}(\omega_c + 2\alpha t)}, \quad -\frac{T}{2} \le t \le \frac{T}{2} \qquad (10)$$

Equation (10) shows the complex IQ data corresponding to reflection from a single object at distance r from the radar. In fact, the radar can detect signals from a continuous range, as shown in Figure 4. When contributions from different points along the continuous detectable range are taken into consideration, equation (10) can be rewritten into integration form as:

$$y(t) = \int_{-\infty}^{\infty} \frac{1}{2} \cdot A(r) \cdot e^{-j\frac{2(\omega_c + 2\alpha t)}{c} r} \cdot dr, \quad -\frac{T}{2} \le t \le \frac{T}{2} \qquad (11)$$

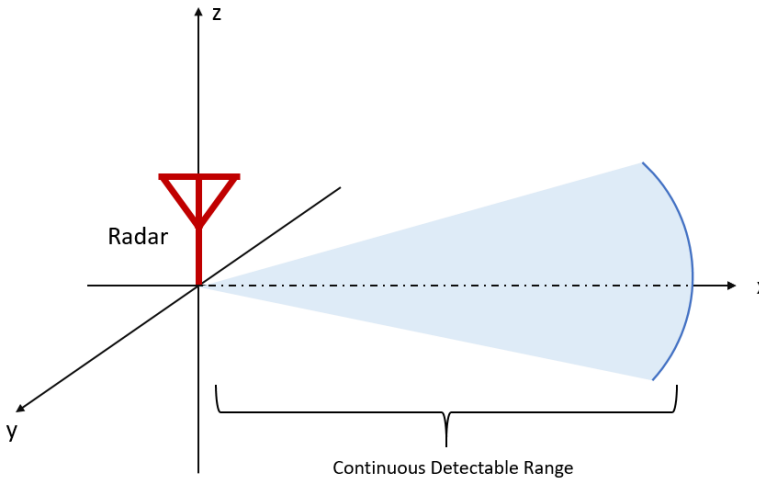

Figure 4: Radar Detectable Range

2.2.2 Fourier Analysis

Definition of Fourier Transform and Inverse Fourier Transform are shown as follows:

$$X(j\omega) = \int_{-\infty}^{\infty} x(t) \cdot e^{-j\omega t} \cdot dt \qquad (12)$$

$$x(t) = \frac{1}{2\pi} \int_{-\infty}^{\infty} X(j\omega) \cdot e^{j\omega t} \cdot d\omega \qquad (13)$$

In equation (11), let $\Omega = \frac{2(\omega_c + 2\alpha t)}{c}$ and $Y(j\Omega) = y(t)$. Equation (11) can be written as:

$$Y(j\Omega) = \int_{-\infty}^{\infty} \frac{A(r)}{2} \cdot e^{-j\Omega r} \cdot \, dr \qquad (14)$$

Comparing equation (14) with (12), observe that $Y(j\Omega)$ and $\frac{A(r)}{2}$ satisfy the Fourier Transform relationship. Therefore, by taking Inverse Fourier Transform (IFT) to $y(t)$, which is equivalent to $Y(j\Omega)$, range profile $A(r)$ can be calculated.

2.2.3 Discrete-Time Signal Model for Single Pulse

In order to use a computer to perform data processing, continuous-time data from radar receiver needs to be converted into discrete-time data. As shown in Figure 3, analog-to-digital converters (ADC) in the radar receiver construct discrete-time signals, $y_I[n]$ and $y_Q[n]$, by sampling continuous-time signals $y_I(t)$ and $y_Q(t)$. Based on $y_I[n]$ and $y_Q[n]$, discrete-time complex IQ data is constructed as:

$$y[n] = y_I[n] + j \cdot y_Q[n]$$

Equivalently, $y[n]$ can be treated as a set of samples from continuous-time complex IQ data $y(t)$.

Discrete-time complex signal $y[n]$ is constructed by taking K equal-space samples from $y(t)$. Taking samples from $y(t)$ only influences terms related to time, t. Therefore, in equation (10), the only term influenced by sampling is $(\omega_c + 2\alpha t)$. Refer to equation (4), $(\omega_c + 2\alpha t)$ is the instantaneous frequency of the transmission signal $s(t)$. As shown in Figure 2, the frequency of $s(t)$ is linearly increased with time. By taking K equal-space samples from $y(t)$, following relationship is satisfied:

$$(\omega_c + 2\alpha t), \quad -\frac{T}{2} \le t \le \frac{T}{2} \xrightarrow{Take\ K\ Equal-Space\ Samples} 2\pi f_{Low} + 2\pi(n-1)\cdot\Delta f\ , \ n = 1,2,\dots,K \qquad (15)$$

where f_{Low} denotes the minimum frequency in a pulse (unit of f_{Low} is Hz), Δf denotes the step frequency. Relationships among the number of samples, K, the bandwidth of the radar system, BW, step frequency Δf and carrier frequency ω_c are:

$$\Delta f = \frac{BW}{(K-1)} \qquad (16)$$

$$f_{Low} = \frac{\omega_c}{2\pi} - \frac{BW}{2} \qquad (17)$$

By substituting the result from equation (15) into equation (10), the discrete-time complex IQ data are:

$$y[n] = \frac{A(r)}{2} \cdot e^{-j\frac{4\pi r \cdot f_{Low}}{c}} \cdot e^{-j2\pi\frac{2r\cdot\Delta f}{c}(n-1)}, \quad n = 1,2,3,\dots,K. \qquad (18)$$

According to analysis in Section 1.2.2, by taking IFT of the signal $y(t)$, information about the range profile $A(r)$ is extracted. $y[n]$ in equation (18) is a discrete-time signal sampled from $y(t)$. In order to extract information about the range profile from $y[n]$, an Inverse Discrete Fourier Transform (IDFT) is applied to $y[n]$. Let $A[m]$ denote the set of equal-space samples of range profile, $A(r)$, in the spatial domain. $A[m]$ is called "discrete-time range profile." The argument, m, represents the index. The relationship between $A(r)$ and $A[m]$ is:

$$A[m] = \frac{A(r)}{2}\Big|_{r=\frac{m-1}{K}\cdot W_r}, \ m = 1,2,3,\dots,K \qquad (19)$$

where, W_r represents the maximum alias-free range extent of the image from radar system. Information about W_r is discussed in section 2.24.

When parameter r in equation (18) is written as $(\frac{m-1}{K} \cdot W_r)$, equation (18) becomes:

$$y[n] = A[m] \cdot e^{-j\frac{4\pi r \cdot f_{Low}}{c}} \cdot e^{-j2\pi\frac{2\cdot(m-1)\cdot W_r\cdot\Delta f}{K\cdot c}(n-1)}, \ n = 1,2,3,\dots,K; \ m = 1,2,3,\dots,K. \qquad (20)$$

Particularly, we keep parameter r in $e^{-j\frac{4\pi r \cdot f_{Low}}{c}}$ in equation (20), for the convenience in next-stage analysis.

2.2.4 Performance of Radar System

Performance of a radar system is determined by radar equations shown as follows:

$$W_r = \frac{c}{2 \cdot \Delta f} \quad (21) \qquad \Delta r = \frac{W_r}{K - 1} \quad (22)$$

$$W_x = \frac{\lambda_{min}}{2 \cdot \Delta\theta} \quad (23) \qquad \Delta x = \frac{\lambda_c}{2 \cdot (N_p - 1) \cdot \Delta\theta} \quad (24)$$

W_r is the maximum alias-free range extent of the image, Δr is the range resolution; W_x is the maximum alias-free cross-range (or azimuth) extent of the image, Δx is the cross-range (or azimuth) resolution. $\Delta\theta$ is the cross-range (or azimuth) step size; λ_{min} is the minimum wave length of the radar, where $\lambda_{min} = \frac{c}{f_{High}} = \frac{c}{f_{Low+BW}}$; λ_c is the center length wave of the radar, where $\lambda_c = \frac{c}{f_c}$; N_p is the number of pulses. A graphical representation of W_r, Δr, W_x and Δx is shown in Figure 5.

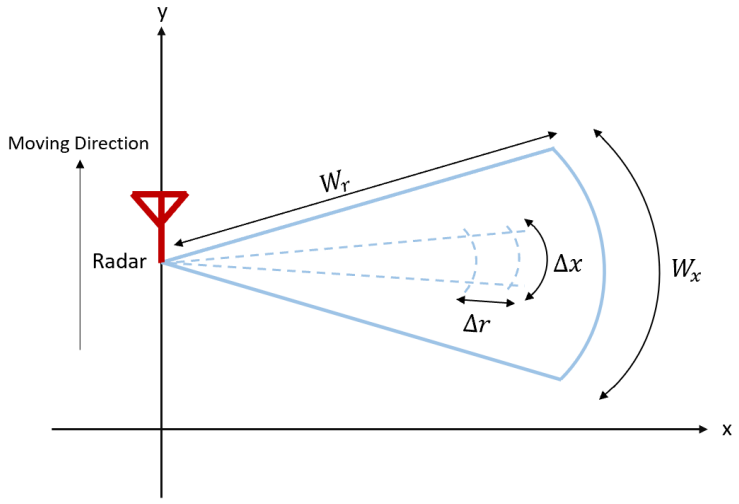

Figure 5: Graphical Representation of Radar Parameters

2.2.5 Range Profile for Single Pulse

The analysis in Section 2.2.3 shows that information about range profile, $A(r)$, can be extracted by taking IDFT of $y[n]$ in equation (20). In MATLAB, the IDFT of a signal X is finished by calling function $ifft(X)$. The definition of function $ifft(X)$ is: [10]

$$x(m) = \frac{1}{K}\sum_{n=1}^{K} X(n) \cdot e^{j\cdot\frac{2\pi}{K}(m-1)(n-1)} \qquad (25)$$

where K is the number of samples.

Applying function $ifft$ to signal $y[n]$ in equation (20), the result is shown as follows:

$$ifft(\,y[n]) = \frac{1}{K}\sum_{n=1}^{K} y[n] \cdot e^{j\cdot\frac{2\pi}{K}(m-1)(n-1)}$$

$$ifft(\,y[n]) = \frac{1}{K}\sum_{n=1}^{K} (A[m] \cdot e^{-j\frac{4\pi r\cdot f_{Low}}{c}} \cdot e^{-j2\pi\frac{2\cdot(m-1)\cdot W_r\cdot\Delta f}{K\cdot c}(n-1)}) \cdot e^{j\cdot\frac{2\pi}{K}(m-1)(n-1)}$$

$$ifft(y[n]) = \frac{1}{K}\sum_{n=1}^{K} A[m] \cdot e^{-j\frac{4\pi r\cdot f_{Low}}{c}} \cdot e^{j2\pi(n-1)(\frac{m-1}{K} - \frac{2\cdot(m-1)\cdot W_r\cdot\Delta f}{K\cdot c})}. \qquad (26)$$

Combining equation (21), $W_r = \frac{c}{2\cdot\Delta f}$, and equation (26) yields:

$$P[m] = \; ifft(y[n]) = \frac{1}{K} \cdot A[m] \cdot e^{-j\frac{4\pi r\cdot f_{Low}}{c}} \sum_{n=1}^{K} e^{j2\pi(n-1)\times 0}$$

$$P[m] = ifft(y[n]) = A[m] \cdot e^{-j\frac{4\pi r\cdot f_{Low}}{c}} \qquad (27)$$

$P[m]$ is the discrete-time range profile of a pulse without phase correction and it is called "pre-correction range profile." By multiplying phase correction term $e^{j\frac{4\pi r\cdot f_{Low}}{c}}$ on both sides of equation (27), it becomes:

$$A[m] = e^{j\frac{4\pi r \cdot f_{Low}}{c}} \cdot P[m] \qquad (28)$$

where $A[m]$ is the discrete-time range profile of a pulse. In equation (28), samples m indexes the range according to:

$$r = \frac{m-1}{K} \cdot W_r \quad m = 1,2,3,\dots,K. \qquad (29)$$

Equation (29) maps the sample index to physical distance between the object and radar.

Alternatively, shown in equation (30), application of the $fftshift()$ command in MATLAB to equation (29) reorganizes the signal and puts $m = 1$ at the center of the range profile. The mapping between the index and physical distance is given by equation (31).

$$A[m] = e^{j\frac{4\pi r \cdot f_{Low}}{c}} \cdot fftshift\{\ ifft(y[n])\ \} = e^{j\frac{4\pi r \cdot f_{Low}}{c}} \cdot fftshift\{\ P[m]\ \} \qquad (30)$$

$$r = \frac{m-1}{K} \cdot W_r \quad m = -\frac{K}{2}, \left(1 - \frac{K}{2}\right), \dots, \left(\frac{K}{2} - 1\right). \qquad (31)$$

By combing equations (19), (28) and (29) (or equations (19), (30) and (31)), the range profile, $A(r)$ can be computed.

"Range line" is a figure describing the relationship between the distance, r and the magnitude of range profile $|A(r)|$. A range line shows information about objects in the detected field. Figure 6 is an example showing the range line for one pulse. Three peaks in Figure 6 correspond to three distinguishable objects in the field; distances from the radar system to three objects are 38.24m, 39.93m and 41.61m.

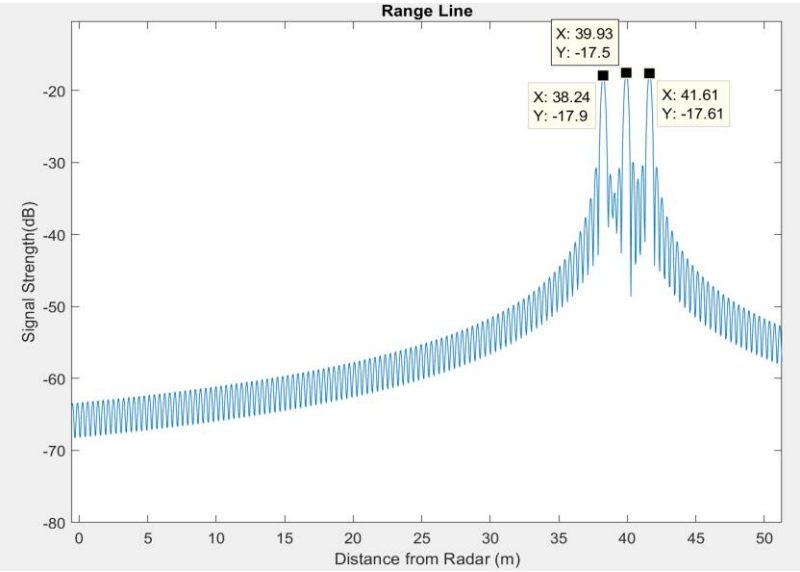

Figure 6: Range Line Example

Table 3: Backprojection Parameter List

Parameter	Type	Description
N_p	integer	number of pulses
$(AntX_k, AntY_k, AntZ_k)$	double	coordinate of radar at k^{th} pulse (m for $AntX$, $AntY$, $AntZ$)
K	integer	number of samples per pulse from radar system
$\boldsymbol{P_k}$	complex vector $1\times K$	pre-correction discrete-time range profile at k^{th} pulse.
$\boldsymbol{A_k}$	complex vector $1\times K$	discrete-time range profile at k^{th} pulse.
E_x	double	x-direction extent (m)
E_y	double	y-direction extent (m)
N_x	integer	number of pixels along x-direction
N_y	integer	number of pixels along y-direction
$(x_{cnt}, y_{cnt}, z_{cnt})$	double	image center coordinate (m for x, y, z)
(x_{pi}, y_{pi}, z_{pi})	double	coordinate of i^{th} pixel (m for x ,y, z)
$\boldsymbol{Im_k}$	complex vector $(N_x \times N_y) \times 1$	image values from k^{th} pulse.
$\boldsymbol{Im_{final}}$	complex vector $(N_x \times N_y) \times 1$	final image value

2.2.6 Backprojection

According to discussion in Sections 2.2.1 to 2.2.5, at a specific location, the radar system sends out a pulse and receives reflected signals from the field. After a series of data processing steps, the discrete-time range profile, $A[m]$, is computed at this location. Backprojection is an algorithm to construct an image by using position information of radar system at each pulse and the discrete-time range profile, $A[m]$, at each pulse. Table 3 shows parameters involved in the backprojection algorithm. Pseudo code of the backprojection algorithm for 2-D image construction is listed as follows:

(1) Compute pre-correction discrete-time range profile for each of N_p pulses. The discrete-time range profile at k^{th} pulse, $P_k[m]$ (k = 1, 2 …N_p.), is calculated by taking $ifft$, according to equation (27).

(2) Specify values of E_X, E_Y, N_X, N_Y and coordinate of image center $(x_{cnt}, y_{cnt}, z_{cnt})$.

(3) Compute coordinates for each pixel in the image based on parameters in Step (2).

(4) Read GPS data to determine radar location coordinates $(AntX_k, AntY_k, AntZ_k)$. (k = 1, 2 …N_p.)

(5) for k = 1 to N_p

for i = 1 to $N_X \times N_Y$

Initialize $Im_k[i]$ to zero

Calculate distance d_i, between $(x_{pi}, y_{p_i}, z_{p_i})$ and $(AntX_k, AntY_k, AntZ_k)$

According to equation (29), calculate index $m_i = \frac{K \cdot d_i}{W_r} + 1$

Find integers $m_1 = floor(m_i)$ and $m_2 = ceiling(m_i)$

Find pre-correction range profile value $P_k[m_1]$ and $P_k[m_2]$

Perform linear interpolation based on $m_1, m_2, P_k[m_1], P_k[m_2]$ and m_i, to compute $P_k[m_i]$

According to equation (28), $A_k[m_i] = P_k[m_i] \cdot e^{j\frac{4\pi \cdot d_i \cdot f_{Low}}{c}}$

$Im_k[i] = A_k[m_i]$

end

end

(6) $\boldsymbol{Im_{final}} = \sum_{k=1}^{N_p} \boldsymbol{Im_k}$. The final image for display is the magnitude, $|\boldsymbol{Im_{final}}|$.

Figure 7 shows a graphical interpretation of the backprojection algorithm. In Figure 7, image values for two pixels are calculated based on radar range profiles at two locations. Figure 7(a) shows the process of distance mapping, and Figure 7(b) shows the calculation of pixel value. A_1, A_2, A_3 and A_4 in the figure are complex numbers.

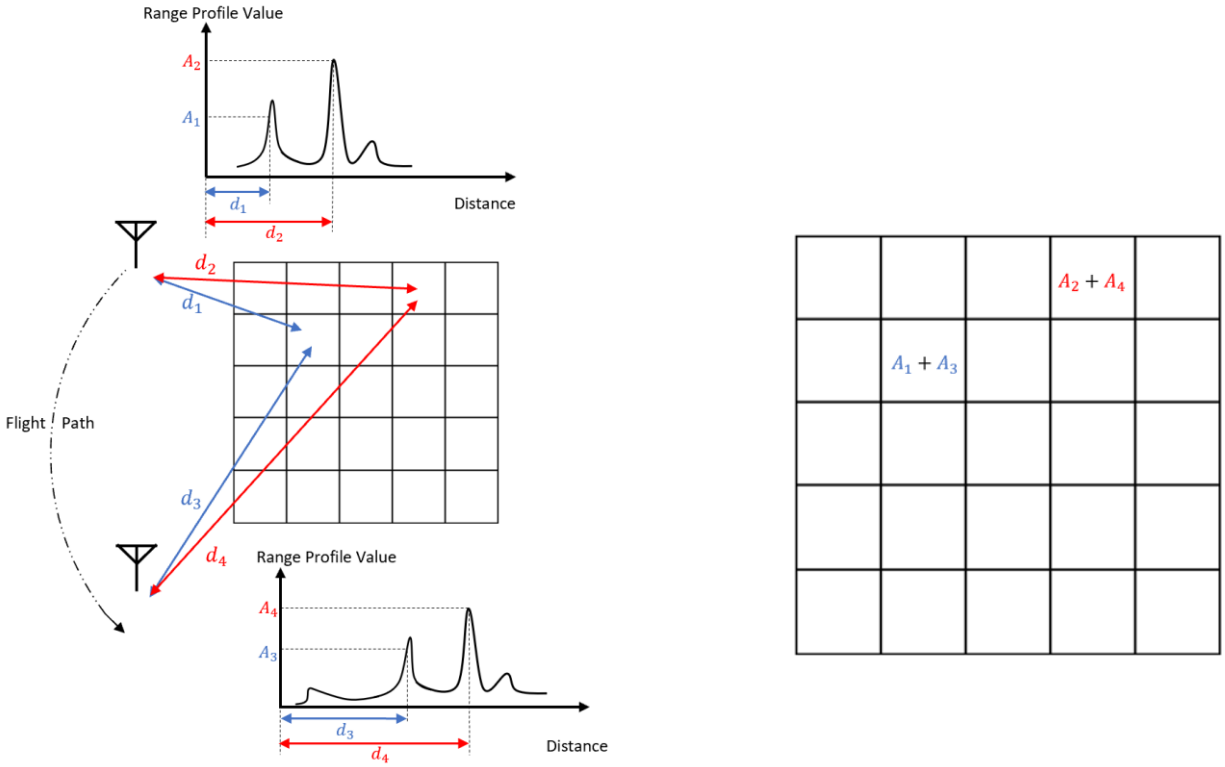

(a) (b)

Figure 7: Backprojection Graphical Interpretation

CHAPTER 3: Autofocus Algorithm

Measurement in SAR system is sensitive to non-ideal factors, such as environmental noises, atmospheric propagation delays in the radar signal, etc. These non-ideal factors smear or blur the SAR image. In order to construct a high-quality SAR image without extra hardware cost, an autofocus algorithm is necessary. In 2012, Joshua N. Ash proposed a SAR autofocus method based on backprojection imaging [8]. The goal of the autofocus method is to maximize the sharpness of the SAR image.

3.1 General Signal Model

The sharpness of the image is defined as:

$$s(\hat{\phi}) = \sum_m \Psi(v_m(\hat{\phi}))$$

where $v_m(\hat{\phi})$ is the intensity of the m^{th} pixel in the image after a set of phase corrections, $\hat{\phi}$ and $\Psi(x)$ is a convex function. $\Psi(x) = x^2$ is a reasonable choice in the algorithm, because it not only provides a closed-form solution for the final result, but also yields maximum likelihood phase error estimation for the model in [8]. Therefore, the sharpness of the SAR image can be determined as:

$$s(\hat{\phi}) = \sum_m \left(v_m(\hat{\phi})\right)^2 = ||\, \boldsymbol{v}\, ||^2 \qquad (32)$$

According to Section 2.2.6, a SAR image can be represented as:

$$\boldsymbol{Im_{final}} = \sum_{k=1}^{N_p} \boldsymbol{Im_k} \qquad (33)$$

where the meaning of parameters N_p, $\boldsymbol{Im_k}$ and $\boldsymbol{Im_{final}}$ are defined in Table 3.

Two assumptions are made in this autofocus algorithm:

1) Influences from non-ideal factors can be modeled as a phase error per pulse:

$$\widetilde{\boldsymbol{Im}_{\boldsymbol{k}}} = \boldsymbol{Im}_{\boldsymbol{k}} \cdot e^{j\phi_k} \qquad (34)$$

where $\boldsymbol{Im}_{\boldsymbol{k}}$ denotes the uncorrupted image value at the k^{th} pulse, $\widetilde{\boldsymbol{Im}_{\boldsymbol{k}}}$ denotes the corrupted image value at the k^{th} pulse and ϕ_k denotes the phase error at the k^{th} pulse.

2) For different values of k, the values of ϕ_k are independent of each other.

The goal of the algorithm is to find a set of optimal phase corrections, $\widehat{\boldsymbol{\phi}} = \{\hat{\phi}_1, \hat{\phi}_2, \dots, \hat{\phi}_{N_p}\}$, so that the sharpness of

$$\widehat{\boldsymbol{Im}_{\boldsymbol{final}}} = \sum_{k=1}^{N_p} \widetilde{\boldsymbol{Im}_{\boldsymbol{k}}} \cdot e^{-j\hat{\phi}_k} \qquad (35)$$

is maximized under the metric shown in equation (32). The optimal phase correction is denoted as:

$$\hat{\phi} = \arg \max_{\phi}(s(\phi)) \,. \qquad (36)$$

According to assumption 2) mentioned above, because the values of ϕ_k are independent of each other for different values of k, each parameter in the set $\widehat{\boldsymbol{\phi}}$ can be optimized in turn, while the rest of parameters are kept unchanged. Optimization over the set $\widehat{\boldsymbol{\phi}}$ can be performed for multiple iterations. We denote the optimal phase correction for the k^{th} pulse in the i^{th} iteration as $\hat{\phi}_k^i$. The optimal phase correction for the k^{th} pulse in the $(i+1)^{th}$ iteration can be represented as:

$$\hat{\phi}_k^{i+1} = \arg \max_{\phi}(s(\hat{\phi}_1^{i+1}, \hat{\phi}_2^{i+1}, \dots, \phi, \hat{\phi}_{k+1}^i, \dots, \hat{\phi}_{N_p}^i)) , \quad k = 1,2, \dots, N_p. \qquad (37)$$

Pseudo code of autofocus algorithm is shown as:

for all iterations

for k = 1 to N_p

Perform single pulse phase correction to k^{th} pulse

end

end

Information about single pulse phase correction is shown in Sections 3.2 to 3.4 below.

3.2 Signal Model for Single Pulse Phase Correction

Following equation (37), for the k^{th} pulse, equation (35) can be rewritten as:

$$\widehat{\boldsymbol{Im}}_{\boldsymbol{final}} = \left(\sum_{p=1}^{k-1} \widetilde{\boldsymbol{Im}}_{\boldsymbol{p}} \cdot e^{-j\hat{\phi}_p^{i+1}} + \sum_{p=k+1}^{N_p} \widetilde{\boldsymbol{Im}}_{\boldsymbol{p}} \cdot e^{-j\hat{\phi}_p^{i}} \right) + \widetilde{\boldsymbol{Im}}_{\boldsymbol{k}} \cdot e^{-j\phi}$$

$$\widehat{\boldsymbol{Im}}_{\boldsymbol{final}} = \boldsymbol{x} + \boldsymbol{y} \cdot e^{-j\phi} \qquad (38)$$

where $\boldsymbol{x} = (\sum_{p=1}^{k-1} \widetilde{\boldsymbol{Im}}_{\boldsymbol{p}} \cdot e^{-j\hat{\phi}_p^{i+1}} + \sum_{p=k+1}^{N_p} \widetilde{\boldsymbol{Im}}_{\boldsymbol{p}} \cdot e^{-j\hat{\phi}_p^{i}})$ and $\boldsymbol{y} = \widetilde{\boldsymbol{Im}}_{\boldsymbol{k}}$.

Relationship between intensity of the m^{th} pixel v_m and its image value, $\widehat{Im}_{final_m}$ is:

$$v_m = |\widehat{Im}_{final_m}|^2 = \widehat{Im}_{final_m} \widehat{Im}^*_{final_m} = (x_m + y_m \cdot e^{-j\phi})(x_m^* + y_m^* \cdot e^{j\phi})$$

$$v_m = \underbrace{|x_m|^2 + |y_m|^2}_{(v_0)_m} + \underbrace{2 \cdot Re(y_m^* x_m e^{j\phi})}_{(v_\phi)_m} \qquad (39)$$

where $(v_0)_m$ is constant and $\left(v_\phi\right)_m$ is related to the phase correction term ϕ. $\left(v_\phi\right)_m$ can be further expanded as:

$$v_\phi = 2 \cdot Re(y_m^* x_m) \cdot cos\phi - 2 \cdot Im(y_m^* x_m) \cdot sin\phi$$

$$v_\phi = a_m \cdot cos\phi + b_m \cdot sin\phi \qquad (40)$$

where $a_m = 2 \cdot Re(y_m^* x_m)$ and $b_m = -2 \cdot Im(y_m^* x_m)$.

Applying equations (39) and (40) to all pixels in the image, we can get:

$$\boldsymbol{v} = \boldsymbol{v_0} + \boldsymbol{a} \cdot cos\phi + \boldsymbol{b} \cdot sin\phi \qquad (41)$$

where $\boldsymbol{v}, \boldsymbol{v_0}, \boldsymbol{a}$ and $\boldsymbol{b}$ are $(N_x \times N_y) \times 1$ vectors.

3.3 Geometric Interpretation for Single Pulse Phase Correction

We can interpret equation (41) in a geometric way, as shown in Figure 8. $(N_x \times N_y) \times 1$ vectors $\boldsymbol{v_0}, \boldsymbol{a}$ and $\boldsymbol{b}$ exist in a vector space $R^{N_x \times N_y}$. Although vectors $\boldsymbol{a}$ and $\boldsymbol{b}$ are not necessarily orthogonal to each other, $(\boldsymbol{a} \cdot cos\phi + \boldsymbol{b} \cdot sin\phi)$ can be treated as an ellipse in a 2-D plane, S, in the vector space of $R^{N_x \times N_y}$. The 2-D plane S is offset from the origin $R^{N_x \times N_y}$ of by $\boldsymbol{v_0}$

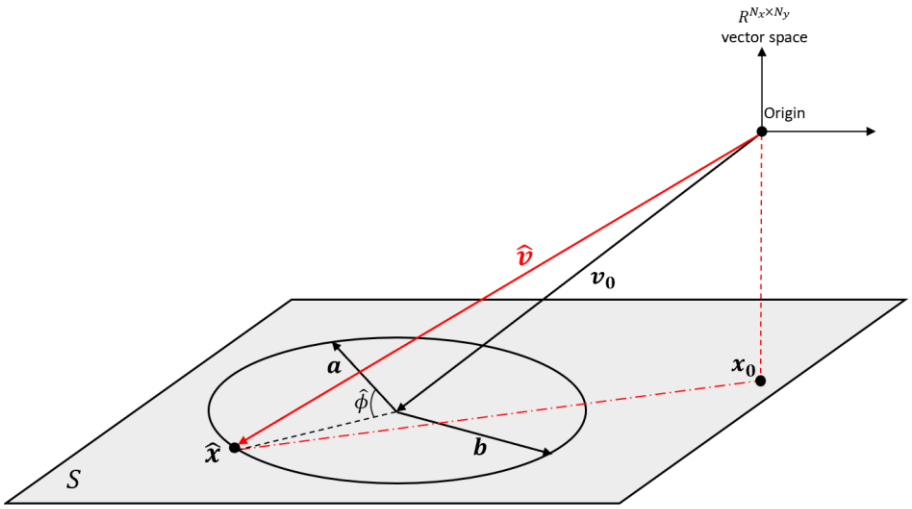

Figure 8: Autofocus Geometric Interpretation for Single Pulse Phase Correction

In equation (32), the sharpness of SAR image is defined as $||\ \boldsymbol{v}\ ||^2$. Maximizing the SAR image sharpness is equivalent to maximizing the magnitude of vector $\boldsymbol{v}$. According to Figure 8, the maximum magnitude of vector $\boldsymbol{v}$ of the can be determined by following steps:

① Project the origin of $R^{N_x \times N_y}$ into 2-D plane S. Denote the projection point as $\boldsymbol{x_0}$.

② Find the optimal focus point $\hat{\boldsymbol{x}}$ on the eclipse, which is farthest away from $\boldsymbol{x_0}$.

③ Determined the optimal phase correction factor $\hat{\phi}$ corresponding to $\hat{\boldsymbol{x}}$.

④ Substitute $\hat{\phi}$ for ϕ in equation (38) to complete single pulse phase correction.

3.4 Phase Optimization for Single Pulse Phase Correction

In this section, we will provide detailed information about the 4-step process mentioned in Section 3.3, which maximizes the sharpness of an image from SAR system. According to Figure 8, the 2-D plane S in vector space of $R^{N_x \times N_y}$ is defined by vectors $\boldsymbol{a}$ and $\boldsymbol{b}$. By performing orthogonalization of $\boldsymbol{a}$ and $\boldsymbol{b}$, we get a basis $\{\boldsymbol{e_1}, \boldsymbol{e_2}\}$ for the S plane:

$$\mathbf{e_1} = \frac{\boldsymbol{a}}{||\boldsymbol{a}||} \qquad \mathbf{e_2} = \frac{\boldsymbol{b} - \boldsymbol{e_1 e_1^T b}}{||\boldsymbol{b} - \boldsymbol{e_1 e_1^T b}||}. \tag{42}$$

In the S plane, $\boldsymbol{a}$ and $\boldsymbol{b}$ become

$$\tilde{\boldsymbol{a}} \equiv \begin{bmatrix} \tilde{a}_1 \\ \tilde{a}_2 \end{bmatrix} = \boldsymbol{E^T a} \qquad \tilde{\boldsymbol{b}} \equiv \begin{bmatrix} \tilde{b}_1 \\ \tilde{b}_2 \end{bmatrix} = \boldsymbol{E^T b} \tag{43}$$

where $\mathbf{E} = [\mathbf{e_1} \ \ \mathbf{e_2}]$. In the original vector space $R^{N_x \times N_y}$, the origin in S plane is offset by vector $\boldsymbol{v_0}$. In a relative perspective, in S plane, the origin of vector space $R^{N_x \times N_y}$ is offset from S plane origin by vector $-\boldsymbol{v_0}$. The projection point of the vector space origin in S plane is $\boldsymbol{x_0}$, determined by:

$$\boldsymbol{x_0} = \boldsymbol{E^T}(\boldsymbol{EE^T})(-\boldsymbol{v_0}) = -\boldsymbol{E^T v_0}. \tag{44}$$

For a point $\boldsymbol{x}$ on the ellipse in the S plane, we denote the normal at this point as $\boldsymbol{n}(\boldsymbol{x})$. For the optimal focus point $\hat{\boldsymbol{x}}$ on the ellipse, the vector $\boldsymbol{x_0} - \hat{\boldsymbol{x}}$ is parallel to the normal at $\hat{\boldsymbol{x}}$, $\boldsymbol{n}(\hat{\boldsymbol{x}})$. This relationship between the vector $\boldsymbol{x_0} - \hat{\boldsymbol{x}}$ and $\boldsymbol{n}(\hat{\boldsymbol{x}})$ can be represented as:

$$\boldsymbol{x_0} - \hat{\boldsymbol{x}} = \alpha\, \boldsymbol{n}(\hat{\boldsymbol{x}}) \qquad (45)$$

where α is an unknown real constant. The parametric equation of the ellipse in the S plane can be written as:

$$f(\boldsymbol{x}) \equiv \boldsymbol{x^T R x} = 1 \qquad (46)$$

with

$$\boldsymbol{x} = \tilde{\boldsymbol{a}}\, cos\phi + \tilde{\boldsymbol{b}}\, sin\phi = [\tilde{\boldsymbol{a}} \quad \tilde{\boldsymbol{b}}] \times \begin{bmatrix} cos\phi \\ sin\phi \end{bmatrix} \qquad (47)$$

$$\boldsymbol{R} = \begin{bmatrix} r_1 & r_3 \\ r_3 & r_2 \end{bmatrix} \qquad (48)$$

$$c = \left(\tilde{a}_2\tilde{b}_1 - \tilde{a}_1\tilde{b}_2\right)^2 \qquad (49)$$

$$r_1 = \frac{\tilde{a}_2^2 + \tilde{b}_2^2}{c} \qquad (50)$$

$$r_2 = \frac{\tilde{a}_1^2 + \tilde{b}_1^2}{c} \qquad (51)$$

$$r_3 = -\frac{\tilde{a}_1\tilde{a}_2 + \tilde{b}_1\tilde{b}_2}{c}\,. \qquad (52)$$

Shown as follows, the normal to the ellipse can be computed by taking the gradient of its parametric equation shown in (46):

$$\boldsymbol{n}(\boldsymbol{x}) \equiv \nabla f(\boldsymbol{x}) = 2\boldsymbol{R}\boldsymbol{x}. \qquad (53)$$

Substituting the result of equation (53) into equation (45) and combining the constant 2 from (53) into the unknown real constant α, we can get:

$$\boldsymbol{x_0} - \hat{\boldsymbol{x}} = \alpha\, \boldsymbol{R}\hat{\boldsymbol{x}}$$

$$\hat{\boldsymbol{x}} = (\alpha \boldsymbol{R} + \boldsymbol{I})^{-1}\, \boldsymbol{x_0} \qquad (54)$$

where $\boldsymbol{I}$ is identity matrix. Eigenvalue decomposition of the matrix $\boldsymbol{R}$ is denoted as $\boldsymbol{R} = \boldsymbol{V}\boldsymbol{\Lambda}\boldsymbol{V^T}$, where $\boldsymbol{\Lambda} = diag(\lambda_1, \lambda_2)$ and λ_1, λ_2 are eigenvalues of matrix $\boldsymbol{R}$. Then, we have

$$(\alpha \boldsymbol{R} + \boldsymbol{I}) = (\alpha \boldsymbol{V}\boldsymbol{\Lambda}\boldsymbol{V^T} + \boldsymbol{I}) = \boldsymbol{V}(\alpha \boldsymbol{\Lambda} + \boldsymbol{I})\boldsymbol{V^T}. \qquad (55)$$

Because $\hat{\boldsymbol{x}}$ is a point on the ellipse defined by equation (47), we can substitute $\hat{\boldsymbol{x}}$ to yield:

$$\hat{\boldsymbol{x}}^{\boldsymbol{T}} \boldsymbol{R} \hat{\boldsymbol{x}} = 1. \qquad (56)$$

Substituting equations (55) and (54) into equation (56), we obtain:

$$1 = \boldsymbol{x_0^T}\, (\alpha \boldsymbol{R} + \boldsymbol{I})^{-1}\, \boldsymbol{R}\, (\alpha \boldsymbol{R} + \boldsymbol{I})^{-1}\, \boldsymbol{x_0}$$

$$1 = \boldsymbol{x_0^T}\, \boldsymbol{V}(\alpha \boldsymbol{\Lambda} + \boldsymbol{I})^{-1} \boldsymbol{V^T} \boldsymbol{R}\, \boldsymbol{V}(\alpha \boldsymbol{\Lambda} + \boldsymbol{I})^{-1} \boldsymbol{V^T}\, \boldsymbol{x_0}$$

$$1 = \boldsymbol{x_0^T}\, \boldsymbol{V}(\alpha \boldsymbol{\Lambda} + \boldsymbol{I})^{-1} \boldsymbol{V^T} \boldsymbol{V}\boldsymbol{\Lambda}\boldsymbol{V^T}\, \boldsymbol{V}(\alpha \boldsymbol{\Lambda} + \boldsymbol{I})^{-1} \boldsymbol{V^T}\, \boldsymbol{x_0}$$

$$1 = \boldsymbol{x_0^T}\, \boldsymbol{V}(\alpha \boldsymbol{\Lambda} + \boldsymbol{I})^{-1} \boldsymbol{\Lambda}\, (\alpha \boldsymbol{\Lambda} + \boldsymbol{I})^{-1} \boldsymbol{V^T}\, \boldsymbol{x_0}$$

$$1 = \boldsymbol{x_0^T}\, \boldsymbol{V} \begin{bmatrix} \frac{\lambda_1}{(\alpha\lambda_1+1)^2} & 0 \\ 0 & \frac{\lambda_2}{(\alpha\lambda_2+1)^2} \end{bmatrix} \boldsymbol{V^T}\, \boldsymbol{x_0} \qquad (57)$$

Let $[\beta_1,\ \beta_2]^T = \boldsymbol{V^T}\, \boldsymbol{x_0}$; then, equation (57) can be written as:

$$\beta_1^2\, \frac{\lambda_1}{(\alpha\lambda_1+1)^2} + \beta_2^2\, \frac{\lambda_2}{(\alpha\lambda_2+1)^2} - 1 = 0 \qquad (58)$$

The roots of equation (58) are the same as the roots of the forth-order polynomial in equation (59) [11].

$$g(\alpha) = \sum_{m=0}^{4} \gamma_m\, \alpha^m \qquad (59)$$

where

$$\gamma_0 = \lambda_1\beta_1^2 + \lambda_2\beta_2^2 - 1 \quad (60)$$

$$\gamma_1 = 2\lambda_1(\lambda_2\beta_2^2 - 1) + 2\lambda_2(\lambda_1\beta_1^2 - 1) \quad (61)$$

$$\gamma_2 = (\lambda_1\beta_1^2 - 1)\lambda_2^2 + (\lambda_2\beta_2^2 - 1)\lambda_1^2 - 4\lambda_1\lambda_2 \quad (62)$$

$$\gamma_3 = -2\lambda_1\lambda_2(\lambda_1 + \lambda_2) \quad (63)$$

$$\gamma_4 = -(\lambda_1\lambda_2)^2. \quad (64)$$

Among the four roots of the fourth-order polynomial in equation (59), the smallest real root corresponds to the farthest distance on the eclipse to the point $\boldsymbol{x_0}$ in the S plane [11]. According to the requirement from Step ② in Section 3.3, we pick up the smallest real root of the polynomial in equation (59) and denote it as $\hat{\alpha}$. Then, we substitute $\hat{\alpha}$ for α in equation (54) to get:

$$\hat{\boldsymbol{x}} = (\hat{\alpha}\boldsymbol{R} + \boldsymbol{I})^{-1}\,\boldsymbol{x_0}. \quad (65)$$

Combining equation (47) with equation (65), we get:

$$\begin{bmatrix} cos\hat{\phi} \\ sin\hat{\phi} \end{bmatrix} = [\tilde{\boldsymbol{a}} \quad \tilde{\boldsymbol{b}}]^{-1}\,(\hat{\alpha}\boldsymbol{R} + \boldsymbol{I})^{-1}\,\boldsymbol{x_0} \quad (66)$$

where $\hat{\phi}$ is the optimal phase correction factor. Based on equation (66), we can get:

$$e^{-j\hat{\phi}} = cos\hat{\phi} - j\,sin\hat{\phi} \quad (67)$$

By substituting equation (67) for $e^{-j\phi}$ in equation (38), single pulse phase correction is completed.

CHAPTER 4: Results

4.1 Software Products

Based on the discussion from Chapter 2 and 3, we implemented a data simulator and image processing software for the SAR system. The processing flows of the data simulator and the image processing software are shown in Figure 9.

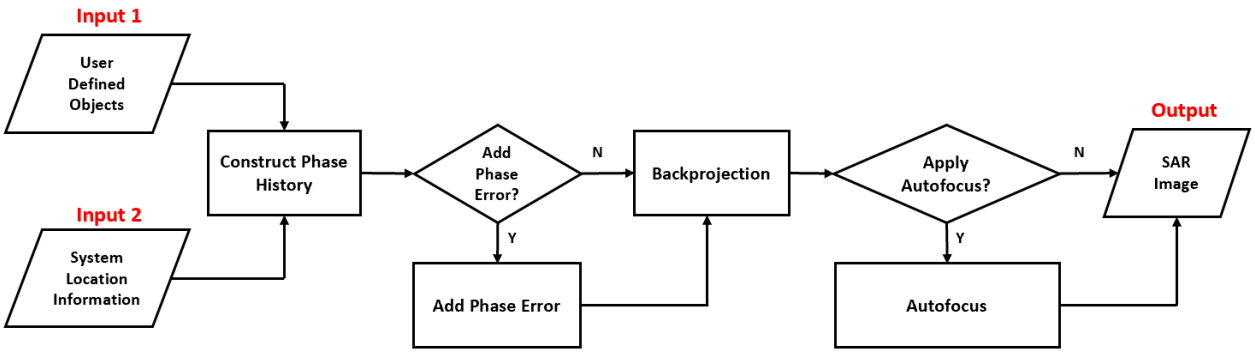

(a)

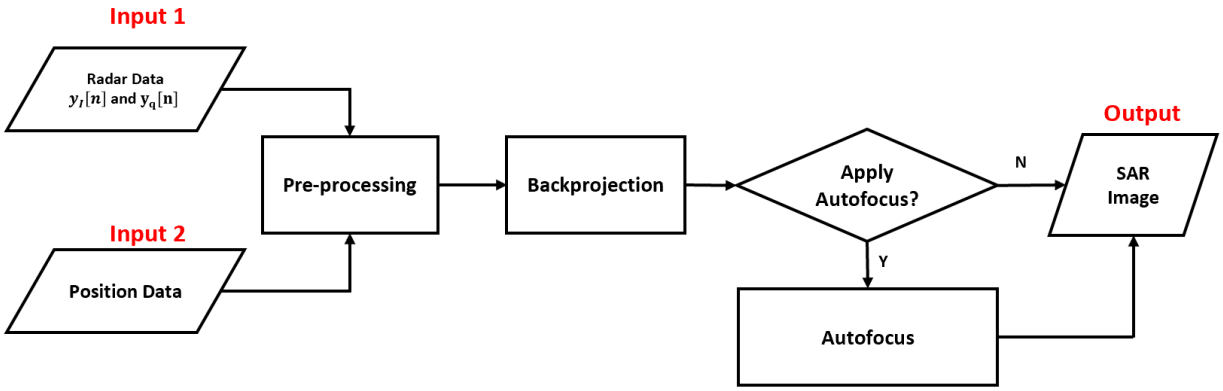

(b)

Figure 9: Software Processing Flow

(a) Data Simulator Processing Flow (b) Image Processing Software Processing Flow

In Figure 9(a), “Input 1” allows the user to defined the number of objects and their locations in the field; for “Input 2,” system location information can either be user-defined or

imported from GPS; information about "Construct Phase History" can be referred from Section 2.1; "Backprojection" in the figure implements information from Section 2.2; information about processes "Add Phase Error" and "Autofocus" is given in Chapter 3.

In Figure 9(b), for "Input 1," signals $y_I[n]$ and $y_Q[n]$ are the same as those mentioned in Figure 3. Position data in "Input 2" can either be imported from GPS or recorded by other hardware devices.

"Pre-processing" in Figure 9(b) consists of two stages. Stage 1, is called "IQ data correction." Ideally, the phase difference between $y_I[n]$ and $y_Q[n]$ is 90°, the magnitude of $y_I[n]$ and $y_Q[n]$ are the same and DC offsets for both $y_I[n]$ and $y_Q[n]$ are zero. However, due to hardware noises, the output signals $y_{I_o}[n]$ and $y_{Q_o}[n]$ from the radar receiver are different from ideal case. "IQ data correction" is a process performing adjustments to $y_{I_o}[n]$ and $y_{Q_o}[n]$, such that the output from the process, $y_{I_c}[n]$ and $y_{Q_c}[n]$ hold the relationship in ideal case. Detailed information about "IQ data correction" is illustrated in Section 5.2. In the second stage of the "Pre-processing," signal $y_{BP}[n]$ is constructed as:

$$y_{BP}[n] = \left(y_{I_c}[n] + j \cdot y_{Q_c}[n]\right) \cdot w[n] \qquad (68)$$

where $y_{I_c}[n]$ and $y_{Q_c}[n]$ are outputs from "IQ data correction" and $w[n]$ is a windowing function [12] to lower sidelobes. The choice of $w[n]$ is subject to hardware performance of radar system, as well as the interference from environment.

4.2 Experimental Results

We conducted a series of experiments to test the performance of the SAR system. In our experiments, we used SDR-KIT 980B Module from Ancortek Inc. as our radar. The radar operates in X-band, with 40° horizontal antenna beam width, 20° vertical antenna beam width, 400MHz bandwidth, 9.8 GHz center frequency, and 1024 samples per sweep. For windowing function mentioned in equation (68), we selected blackman window. Therefore, after "Pre-Processing" in Figure 10(b), we had:

$$y_{BP}[n] = \left(y_{I_c}[n] + j \cdot y_{Q_c}[n]\right) \cdot blackman[n] \qquad (69)$$

where $blackman[n]$ was blackman windowing function [13]. Then, we substituted $y_{BP}[n]$ in equation (69) for $y[n]$ in equation (28) or (30) for backprojection.

4.2.1 Backprojection Experiment

Shown in Figure 10(a), we setup three aluminum reflectors with different shapes and sizes on a soccer field. We put the SAR system on an 80-cm straight rail, which provided accurate location information. The conceptual graph in Figure 10(b) shows the relative positions among the reflectors and the SAR system movement. By using the accurate SAR system location information from the rail, a simulated image was constructed through backprojection, as shown in Figure 10(c). Then, we computed an image shown in Figure 10(d) through backprojection in the image processing software, by combining experimental data from the radar and location information from the rail. Both simulated and experimental images consisted of 201×201 pixels and both of them were displayed in a 40dB dynamic range.

In the computed image, three reflectors can be clearly identified. Relative positions among three reflectors in the computed image were similar those in the simulated image. Signal

strengths from the three reflectors in the simulated image were the same, while signal strengths from the three reflectors in experimental image were different. This was reasonable, because the simulator focused on displaying reflectors on correct positions and it ignored sizes and shapes of reflectors, as well as signal decay associated with the distance. In reality, signal strength from a reflector is subject to its size, its shape, and its distance from radar. The position coordinates of three reflectors in the simulated image were (10, 1.08), (15, -0.96) and (25, 0.12), while in the experimental image, their corresponding coordinates were (11.6, 0.24), (17, -2.34) and (27.5, -2.1). Compared to reflectors in the simulated image, the absolute position of each reflector in the experimental image was shifted to the right in the range direction and shifted down in the cross-range direction.

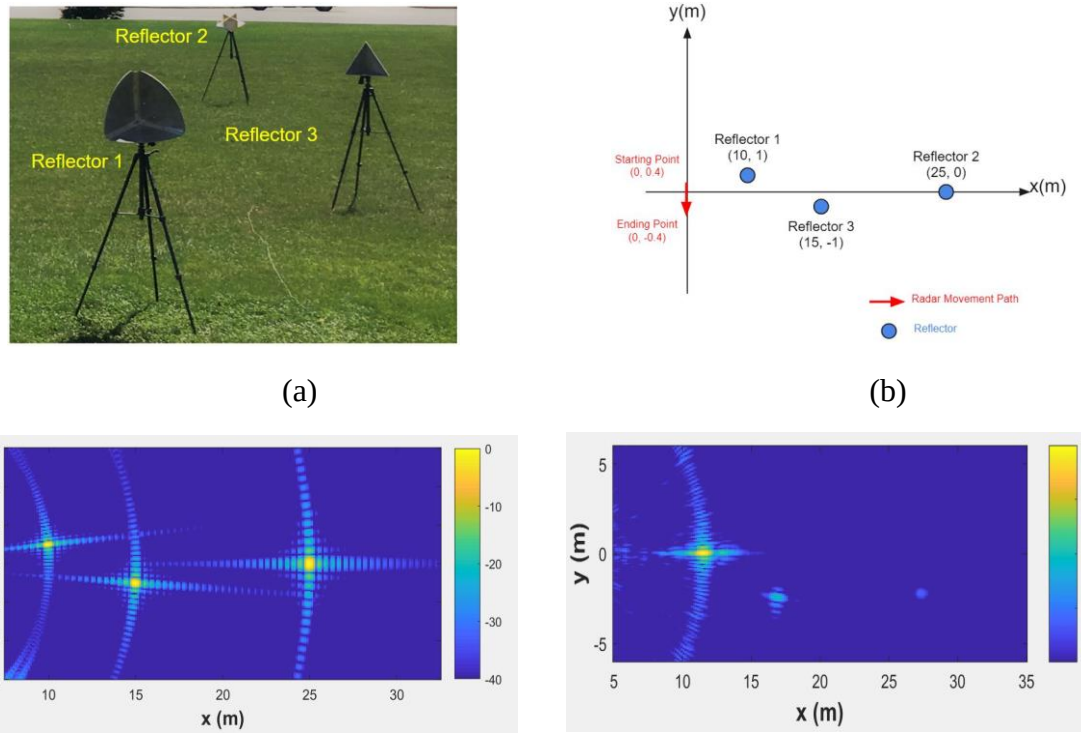

(a) (b)

(c) (d)

Figure 10: Backprojection Experiment

(a) Physical Setup of Reflectors (b) Conceptual Graph

(c) Simulated SAR Image (d) Experimental SAR Image

4.2.2 Autofocus Experiment

In this part of the experiment, we tested the effect of the autofocus algorithm through simulation, as shown in Figure 11. Figure 11(a) is a conceptual graph showing the relative positions among the reflectors and the movement of SAR system. The movement of the system is a simulated flight path consisted of 300 position points. As the SAR system moved along the simulated flight path, it constructed a phase history based on information from 300 positions. We added a random phase error to the data by:

$$y_{k_{err}}[n] = y_k[n] \cdot e^{j\phi_{k_{err}}} \qquad (70)$$

where $y_k[n]$ is the phase history from the k^{th} position on the flight path, $\phi_{k_{err}}$ is the phase error added to $y_k[n]$ and it is a random number between 0 to 2π. After applying equation (70) to phase history from all positions, a corrupted phase history $\boldsymbol{y_{err}} = [\boldsymbol{y_{1_{err}}}, \boldsymbol{y_{2_{err}}}, \cdots, \boldsymbol{y_{300_{err}}}]$ was built. We passed the corrupted phase history $\boldsymbol{y_{err}}$ into backprojection algorithm and simulator produced an image shown in Figure 11(b). Then we applied autofocus to the image in Figure 11(b), and the result was shown in Figure 11(c). Both images in Figure 11(b) and (c) consisted of 201×201 pixels and both of them were displayed in a 20dB dynamic range**.**

In Figure 11(b), no reflector could be identified, because random phase noise smeared the SAR image. Shown in Figure 11(c), application of autofocus removed the negative influence from random phase noise and improved the quality of SAR image significantly.

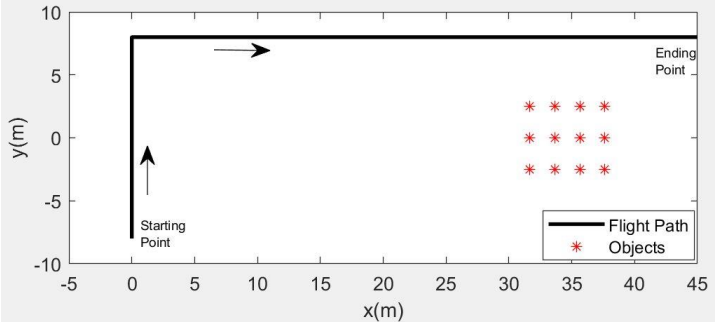

(a)

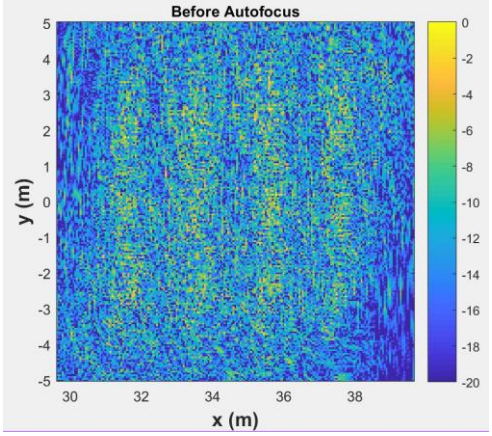

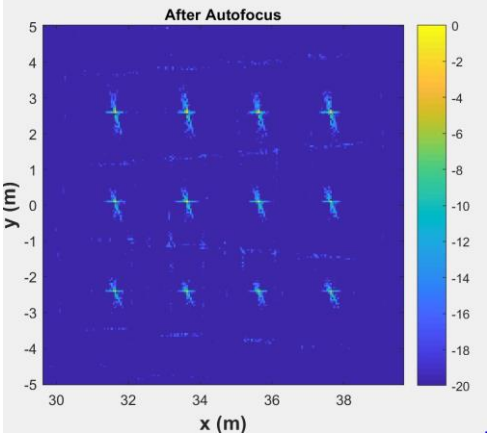

(b) (c)

Figure 11: Autofocus Experiment

(a) Conceptual Graph (b) Simulated SAR Image with Phase Errors

(c) Simulated SAR Image with Autofocus

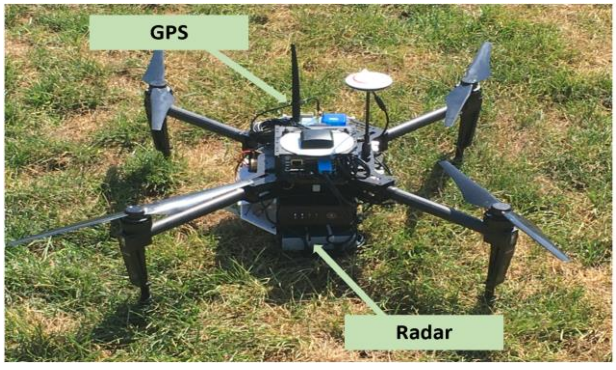

Figure 12: Drone-SAR System

4.2.3 Drone-SAR Experiment

As shown in Figure 12, the design team built the drone-SAR system by integrating the radar, the GPS and other control units on a DJI Matrice 100 Quadcopter drone. We put one steel reflector on the soccer field and flew the drone-SAR system around the reflector at a height between 9 and 10 meters above the ground. Figure 13(a) is a conceptual graph showing the

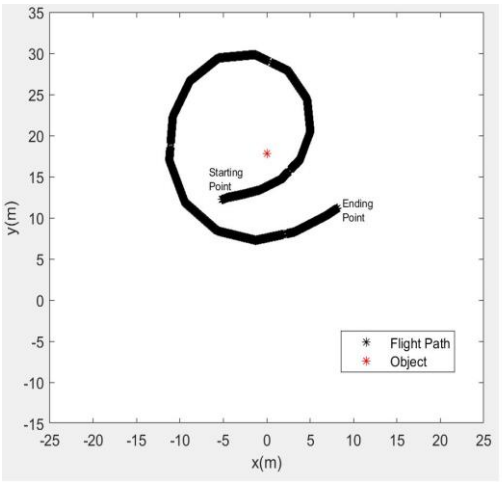

(a)

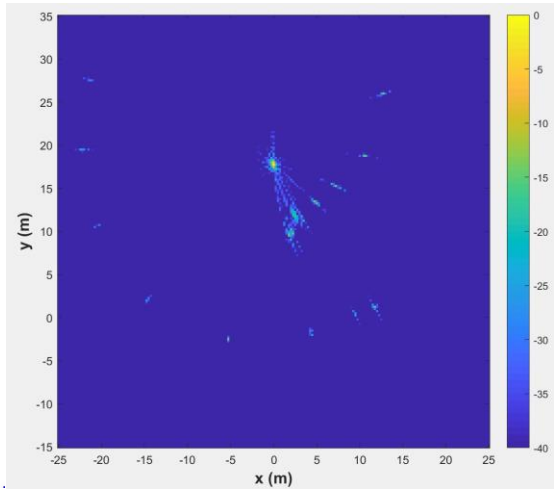

(b)

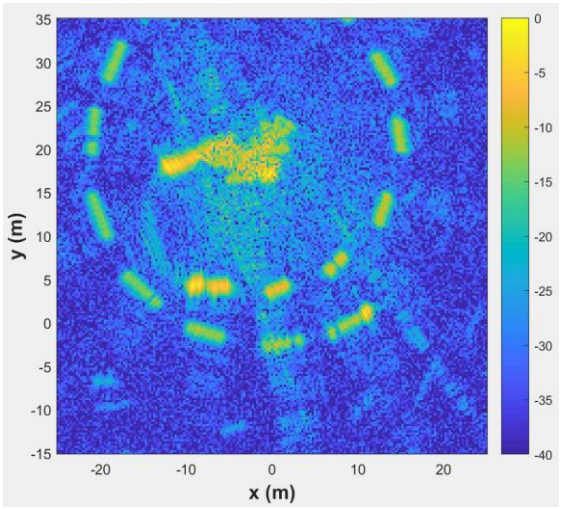

(c)

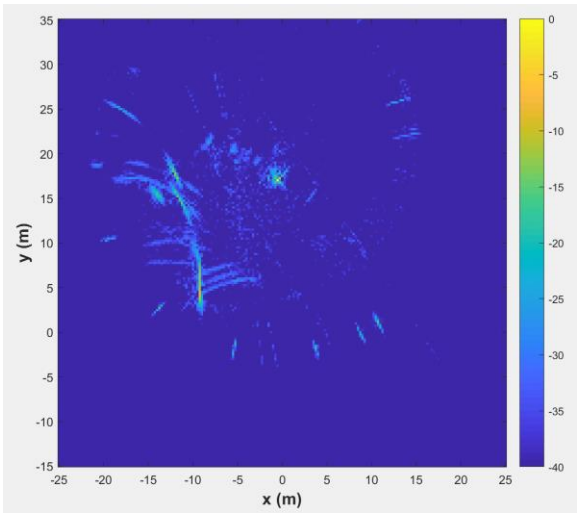

(d)

Figure 13: Drone-SAR Experiment

(a) Conceptual Graph in a Bird's Eye View (b) Simulated SAR Image

(c) Experimental SAR Image without Autofocus (d) Experimental SAR Image with Autofocus

relative position between the reflector and the drone-SAR system in a bird's eye view. By using GPS data as location information, a simulated image was constructed, as shown in Figure 13(b). In the image processing software, we built an image shown in Figure 13(c) by combining experimental data from the radar and location information from the GPS. Then, we applied autofocus to the image in Figure 13(c) and the result was shown in Figure 13(d). All images in Figures 13(b), (c) and (d) consisted of 201×201 pixels and both of them were displayed in a 40dB dynamic range.

Figure 13(c) contained information in two aspects: a blurred region in the middle and a set of rectangular artifacts. The rectangular artifacts were aliases of signals in the middle region and the distribution of these artifacts was similar to the shape of the system flight path shown in Figure 13(a). The region in the middle was what we were interested in, because the reflector was included in it. During the experiment, the data from drone-SAR system was susceptible to errors. The errors could be caused by either imperfection of hardware in drone-SAR system, or interference from the environment. Because of the errors, in Figure 13(c), the middle region of the SAR image was blurred and we could not identify the reflector. Autofocus made important improvements to In Figure 13(d), after applying autofocus, although there were still remaining artifacts in the SAR image, the reflector could be clearly identified.

CHAPTER 5: Error and Analysis

5.1 Ghost Peak in Near-field

In order to have a further study of radar internal noise, we performed a series of tests of our radar in anechoic chamber at ElectroScience Lab (ESL) at OSU. During the test, we did not put any reflector in the anechoic chamber. We ran the radar at a fixed position, collected data for 1000 pulses and plotted the range lines corresponding to these 1000 pulses on a graph, as shown in Figure 14. According to Figure 14, peaks of high magnitude values were observed within the range of 6 meters. Peaks in the range line indicated the existence of reflectors, and these reflectors were located within 6 meters from the radar, although in reality, there was no reflector in the field. We denoted these peaks within 6 meters as "ghost peaks."

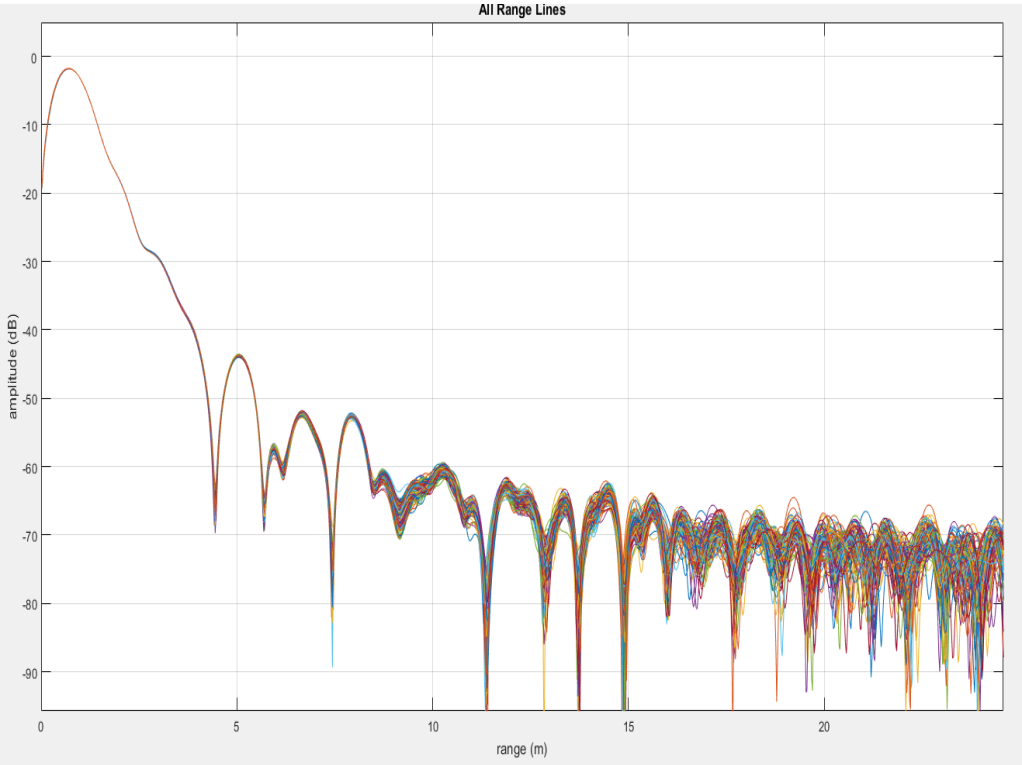

Figure 14: Experimental Range Line in Anechoic Chamber

A possible cause of ghost peaks in the range line was the leakage of transmission signal. In our radar system, the transmitting antenna and receiving antenna were close to each other. When the transmitting antenna sent out a signal, a portion of the transmission signal went directly to the receiving antenna within a short time delay, which likely contributed to ghost peaks in the range line. Since ghost peaks always occurred within 6 meters from radar, in order to remove the influence of ghost peaks on SAR image, we preprocessed the range profile data before backprojection. Pseudo code of the preprocessing is shown as follows:

for k = 1 to N_p

According to equation (32), calculation index $m_k = \frac{K \cdot 6}{W_r} + 1$

Find integers $m_2 = ceiling(m_k)$

for p = 1 to m_2

$A_k[p] = 0$

end

end

The drone-SAR experiment in Section 4.2.3 included the preprocessing mentioned above.

5.2 IQ Imbalance and IQ Correction

5.2.1 Influence of IQ Imbalance

According to Figure 3, equation (7), equation (8) and descriptions in Section 2.1.3, in ideal case, output signals from I and Q channels from radar receiver have the follow form:

$$y_I = A \cdot \cos(x) \qquad (71)$$

$$y_Q = -A \cdot \sin(x) \qquad (72)$$

where $A = \frac{A(r)}{2}$ and $x = \frac{2r}{c}(\omega_c + 2\alpha t) - \frac{4\alpha r^2}{c^2}$. The ideal complex IQ data is computed by:

$$y = y_I + j \cdot y_Q = A \cdot e^{-jx} \qquad (73)$$

In ideal case, signal y_I and y_Q have the same magnitude, zero DC offset and a 90° phase difference. However, due to errors in the radar hardware, the actual output signals from I and Q channels are different from ideal case, and we denote this kind of phenomenon as "IQ imbalance". When IQ imbalance are taken into account, output signals from I and Q channels can be modeled as:

$$\widetilde{y_I} = A \cdot \cos(x) + C \qquad (74)$$

$$\widetilde{y_Q} = -A\alpha \cdot \sin(x + \theta) + D \qquad (75)$$

where $\widetilde{y_I}$ and $\widetilde{y_Q}$ represent the corrupted I and Q signals; θ represents a phase error; C and D represent DC offsets in I and Q channels. Based on $\widetilde{y_I}$ and $\widetilde{y_Q}$, the corrupted complex IQ signal can be represented as:

$$\tilde{y} = \widetilde{y_I} + j \cdot \widetilde{y_Q}$$

$$\tilde{y} = A \cdot \cos(x) - j \cdot A\alpha \cdot cos\theta \cdot \sin(x) - j \cdot A\alpha \cdot sin\theta \cdot \cos(x) + (C + jD). \qquad (76)$$

replace $\cos(x)$ and $\sin(x)$ in equation (75) with $\frac{e^{jx} + e^{-jx}}{2}$ and $\frac{e^{jx} - e^{-jx}}{2}$, equation (76) can be rewritten as:

$$\tilde{y} = Ae^{-jx} \cdot \underbrace{\left[\frac{1}{2} + j \cdot \frac{\alpha}{2}(cos\theta - sin\theta)\right]}_{\beta_1 \cdot e^{j\phi_1}} + Ae^{jx} \cdot \underbrace{\left[\frac{1}{2} - j \cdot \frac{\alpha}{2}(cos\theta + sin\theta)\right]}_{\beta_2 \cdot e^{j\phi_2}} + \underbrace{(C + j \cdot D)}_{\beta_3 \cdot e^{j\phi_3}}$$

$$\tilde{y} = Ae^{-jx} \cdot \beta_1 e^{j\phi_1} + Ae^{jx} \cdot \beta_2 e^{j\phi_2} + \beta_3 e^{j\phi_3}. \qquad (77)$$

To have a further understanding to the difference between equation (73) and (77), we provide the following conceptual example: assume in the ideal case, there is one object located r_0 meters

away from the SAR system. Range lines associated with the ideal complex signal, y and corrupted complex signal, $\tilde{y}$ are plotted, as shown in Figure 15.

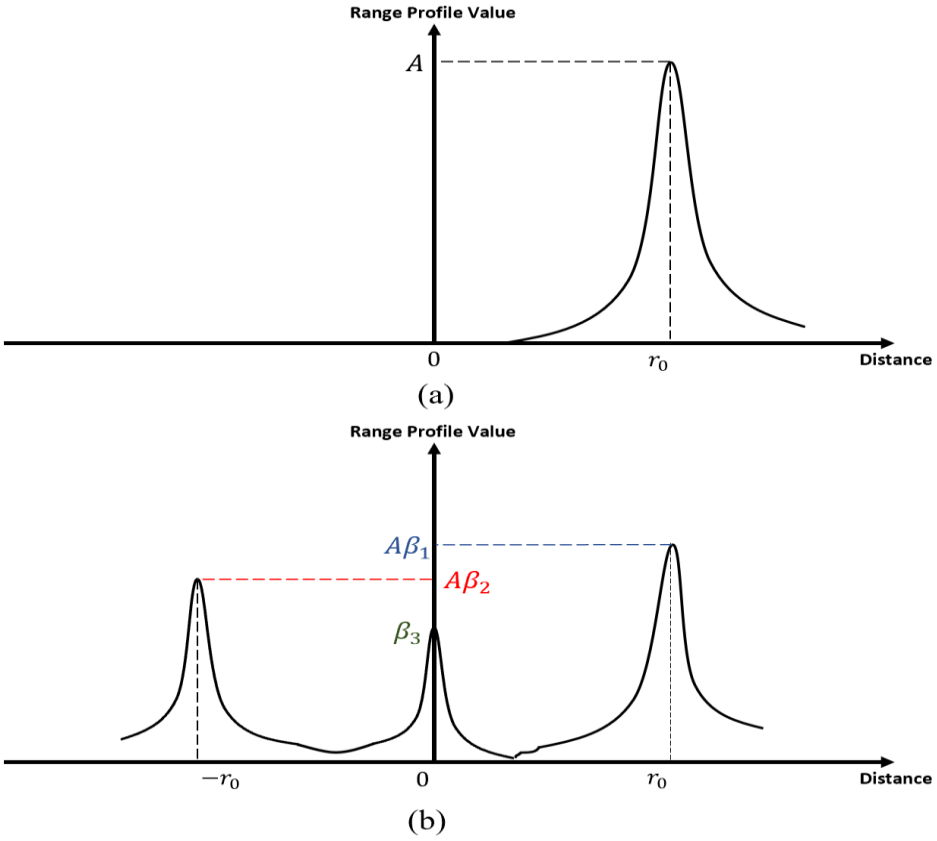

Figure 15: Range Line Analysis

(a) Range Line Associated with Signal y. (b) Range Line Associated with Signal $\tilde{y}$.

Two significant differences between Figure 15(a) and (b) are observed. Firstly, the peak signal strength from the object located at r_0 is attenuated by a factor of β_1; Secondly, in Figure 15(b), there are two additional peaks located at 0 and $-r_0$ meters away from the SAR system. There are no objects in the field corresponding to these two peaks, and therefore, similar to Section 5.1, we also denote these two peaks as "ghost peaks". The third term, $\beta_3 e^{j\phi_3}$, in equation (77) is the source of the ghost peak located at 0; the second term, $Ae^{jx} \cdot \beta_2 e^{j\phi_2}$, in equation (77) contributes to the ghost peak located at $-r_0$ meters away from the SAR system and it is the alias

of the object located at r_0. In addition, the term $e^{j\phi_1}$ in equation (77) brings a phase error to the ideal reflection signal, which is not shown in Figure 15.

5.2.2 IQ Correction

Based on equation (74) and (75), the goal of IQ correction is to remove the influence of C, D, α and θ. We denote T as the period of signal $\cos(x)$ and $\sin(x)$ from equations (73) and (74). IQ correction is performed following equations (78) to (85).

$$y_{I_{avg}} = \frac{1}{N \cdot T}\int_{NT} \widetilde{y_I}(x)\, dx = C \quad (78)$$

$$y_{Q_{avg}} = \frac{1}{N \cdot T}\int_{NT} \widetilde{y_Q}(x)\, dx = D \quad (79)$$

$$VarI = \frac{1}{N \cdot T}\int_{NT} \left(\widetilde{y_I}(x) - y_{I_{avg}}\right)^2 dx = \frac{A^2}{2} \quad (80)$$

$$VarQ = \frac{1}{N \cdot T}\int_{NT} \left(\widetilde{y_Q}(x) - y_{Q_{avg}}\right)^2 dx = \frac{A^2\alpha^2}{2} \quad (81)$$

$$CovIQ = \frac{1}{N \cdot T}\int_{NT} (\widetilde{y_I}(x) - y_{I_{avg}})(\widetilde{y_Q}(x) - y_{Q_{avg}})\, dx = -\frac{A^2\alpha}{2}\sin\theta \quad (82)$$

$$Temp_1 = \sqrt{\frac{VarQ}{VarI} - \left(\frac{CovIQ}{VarI}\right)^2} = \alpha \cdot cos\theta \quad (83)$$

$$Temp_2 = -\frac{CovIQ}{VarI \cdot Temp_1} = tan\theta \quad (84)$$

$$\begin{bmatrix} y_{I_c}(x) \\ y_{Q_c}(x) \end{bmatrix} = \begin{bmatrix} 1 & 0 \\ Temp_2 & \frac{1}{Temp_1} \end{bmatrix} \begin{bmatrix} \widetilde{y_I}(x) - y_{I_{avg}} \\ \widetilde{y_Q}(x) - y_{Q_{avg}} \end{bmatrix} = \begin{bmatrix} 1 & 0 \\ tan\theta & \frac{1}{\alpha \cdot cos\theta} \end{bmatrix} \begin{bmatrix} \widetilde{y_I}(x) - C \\ \widetilde{y_Q}(x) - D \end{bmatrix} \quad (85)$$

where N in equations (78) to (82) is a positive integer; the lengths of integral interval in equations (78) to (82) are NT. In theory, after the IQ correction, $y_{I_c}(x)$ and $y_{Q_c}(x)$ in equation (85) are equal to ideal I and Q signals in equations (71) and (72).

To verify the functionality of IQ correction, we performed a set of simulations. Single-frequency sinusoidal signals with periods of 4.5 seconds and magnitudes of 5 were selected as ideal I and Q signals according to equation (71) and (72). The ideal signal I and Q signals are shown in Figure 16(a). According to equation (74) and (75), IQ imbalance parameters C, D, α and θ were set to -2, -1, 0.8 and $\frac{\pi}{6}$ respectively. Under the influence of the IQ imbalance, the corrupted I and Q signals are shown in Figure 16(b). After IQ correction, the output I and Q signals are shown in Figure 16(c). The relative errors between the ideal IQ signals and the output

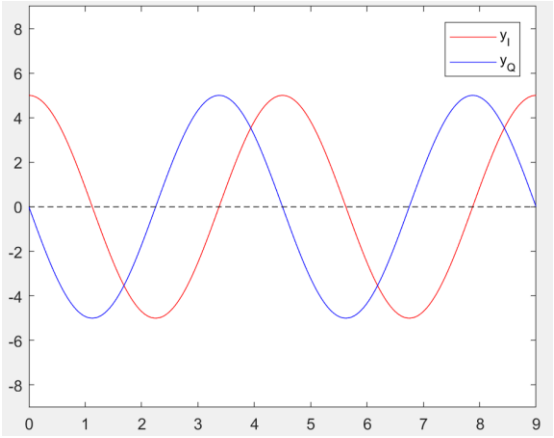

(a)

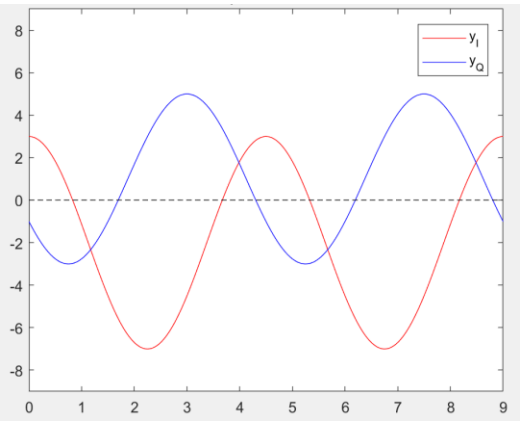

(b)

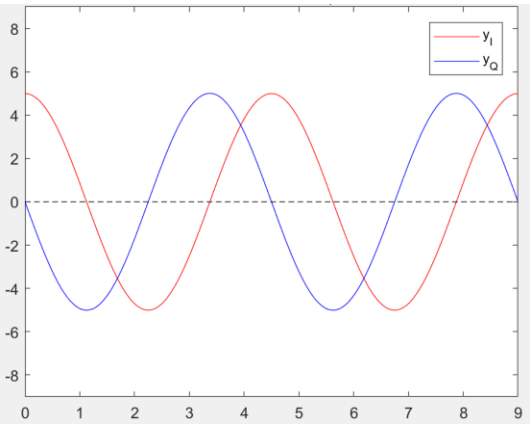

(c)

Figure 16: IQ Correction Simulation

(a) I and Q Signals in the Ideal Case (b) Imbalanced I and Q Signals

(c) IQ Correction Outputs

signals from IQ correction were lower than 1.5%, which means the IQ correction was able to provide an acceptable result.

5.3 Linear Range Error

In previous experiments, we observed reflector position errors in the range direction. As seen in Figure 10, the absolute reflector positions from the experimental image were shifted to the right in range from their expected positions in the simulated image. To have a further understanding about reflector position error in range direction, we conducted the following experiment:

(1) Fix the radar at a specific position on soccer field.

(2) Set a steel reflector at the same height as radar and move the reflector away from radar.

(3) Set down the distance between radar and reflector as r.

(4) Run the radar and collect data for 1000 pluses.

(5) Plot the range line by using experimental data from radar.

(6) Identify the peak corresponding to the reflector on the range line and record its distance from the radar as r_{ex}.

(7) Calculate the range error by $\Delta r = r_{ex} - r$ and record the value of Δr.

(8) Move the reflector to a new position and repeat steps (3) to (7).

By moving around the reflector to different positions, we got different pairs of r and Δr. Figure 17 shows the relationship between r and Δr.

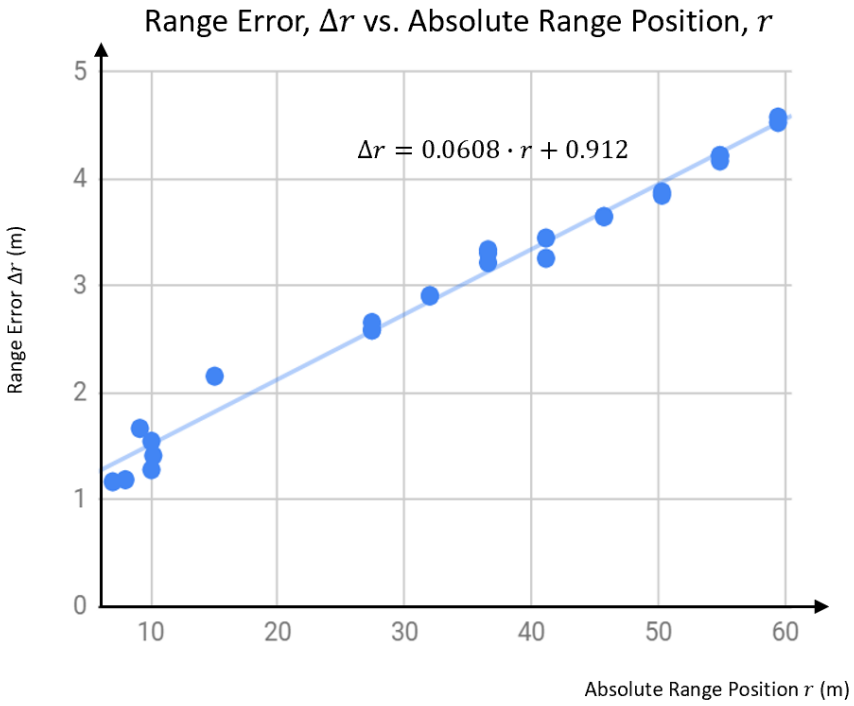

Figure 17: Relationship between Range Error and Reflector Absolute Range Position

To model the range error from this experiment, we should make references to equations about range mapping. By combining equations (21) and (29), the ideal range value can be calculated as:

$$r = \frac{m-1}{K} \cdot \frac{c}{2 \cdot \Delta f} \qquad (86)$$

where K is the number of samples per sweep; m is an integer between 1 and K. In the ideal case, during the sampling process, K equally-spaced samples are taken across the bandwidth of FMCW signal, which contributes to a constant step frequency Δf, between two adjacent points among K samples. However, due to the actual chirp rate, experimental step frequency can be modeled as: $\Delta f_{ex} = \Delta f + \Delta f_{err}$, where Δf_{err} is a constant frequency error. Also, inside the radar system, signals travel through wires and other electronic devices, which contribute to delays in

signal communication. Delays in signal communication bring inaccuracies in range mapping and therefore result in range errors. Since the hardware architecture of radar system is fixed, we can model the hardware delays as a constant factor r_0. Combining the discussions above, we can model the experimental range value, r_{ex} as:

$$r_{ex} = \frac{m-1}{K} \cdot \frac{c}{2 \cdot (\Delta f + \Delta f_{err})} + r_0 \qquad (87)$$

Mathematical expression of Δr in Figure 15 can be gained by subtracting r in equation (86) from r_{ex} in equation (87) and the slope in Figure 17 contains information about Δf_{err} while the intercept is related to r_0.

The weakness of this range error experiment was that at each position, we only measured r and r_{ex} for one time, rather than took multiple measurements and calculated the average. If the linear relationship between range and range error were verified by more reliable experiments, the range error would be removed by incorporating the linear relationship into the image processing software, as correction to r_0 and Δf.

5.4 Motion Error

In the SAR system, an accurate motion measurement is necessary to the constructions of high-quality images. In this project, GPS unit is responsible for the motion measurement. However, GPS unit in the SAR system is susceptible to errors. Errors in GPS data are called "motion errors," which bring attenuations to the qualities of SAR images. Figure 18 shows the influence of motion error to the SAR system.

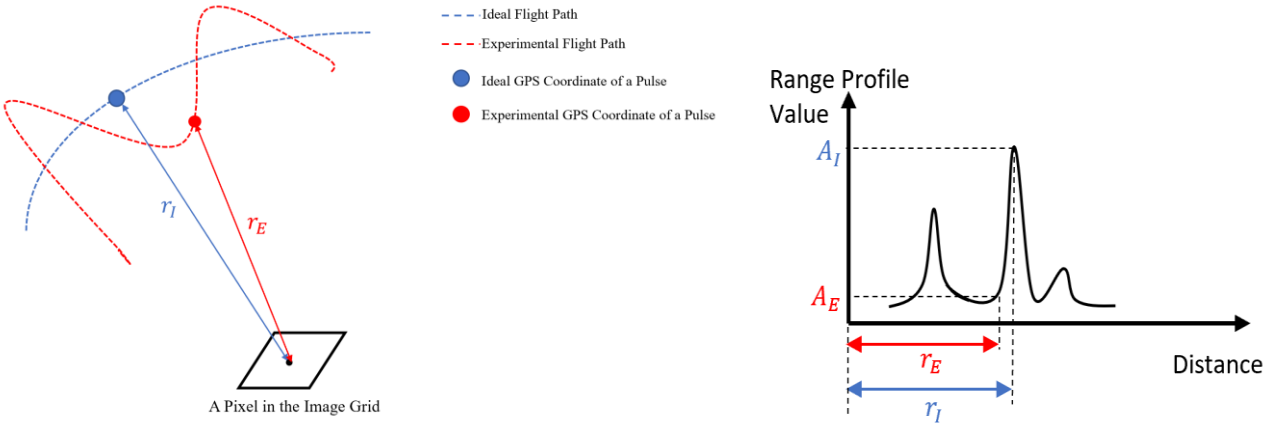

(a) (b)

Figure 18: Influence of the Motion Error

(a) Geometric Representation of the Motion Error.

(b) Influence of the Motion Error on the Range Profile.

In Figure 18(a), the distance between the pixel and the ideal GPS coordinate of a pulse is denoted as r_I; the distance between the pixel and the experimental GPS coordinate of the same pulse is denoted as r_E. As shown in Figure 18(b), a small difference between r_I and r_E (a small error in motion measurement) can bring a significant error to the image value computation of the selected pixel during the backprojection. The SAR image is smeared, when this kind of error is applied to every pixel in the image grid.

In this section of the report, we quantify the influence of the motion error based on equations (27) to (29), as well as description in backprojection algorithm shown in Section 2.2.6. In equation (29), we rewrite the parameter of r in equation (28) in terms of parameter m, so that equation (28) becomes:

$$A[m] = P[m] \cdot e^{j \cdot \frac{4\pi f_{Low}}{c \cdot K} \cdot W_r \cdot (m-1)}, \ m = 1,2,3,\dots,K. \qquad (88)$$

In ideal case for a single pixel shown in Figure 18(a), the distance between a selected pixel and the SAR system is r_I. According to equation (29), the index, m_I, corresponding to r_I is:

$$m_I = \frac{r_I K}{W_r} + 1. \quad (89)$$

Therefore, the ideal image value of the selected pixel is:

$$Im = A[m_I] = P[m_I] \cdot e^{j \cdot \frac{4\pi f_{Low}}{c \cdot K} \cdot W_r \cdot (m_I - 1)}. \quad (90)$$

In Figure 18(a), the experimental distance between a selected pixel and the SAR system is r_E. The relationship between r_E and r_I can be expressed as:

$$r_E = r_I + \Delta r. \quad (91)$$

The index, m_E corresponding to r_E can be computed by equation (29):

$$m_E = \frac{r_E K}{W_r} + 1 \quad (92)$$

$$m_E = \frac{r_I K}{W_r} + 1 + \frac{\Delta r \cdot K}{W_r} = m_I + \frac{\Delta r \cdot K}{W_r}. \quad (93)$$

The experimental image value of the selected pixel is:

$$\widetilde{Im} = A[m_E] = P[m_E] \cdot e^{j \cdot \frac{4\pi f_{Low}}{c \cdot K} \cdot W_r \cdot (m_E - 1)}. \quad (94)$$

Rewrite m_I in equation (90) in terms of m_E according to equation (93), equation (90) becomes:

$$Im = P[m_E - \frac{\Delta r \cdot K}{W_r}] \cdot e^{j \cdot \frac{4\pi f_{Low}}{c \cdot K} \cdot W_r \cdot (m_E - 1)} \cdot e^{-j \frac{4\pi f_{Low} \Delta r}{c}} \quad (95)$$

By combining equations (95) and (94), the result is:

$$\frac{Im}{\widetilde{Im}} = \frac{P[m_E - \frac{\Delta r \cdot K}{W_r}] \cdot e^{-j\frac{4\pi f_{Low}\Delta r}{c}}}{P[m_E]}$$

$$Im = \widetilde{Im} \cdot \underbrace{\frac{P[m_E - \frac{\Delta r \cdot K}{W_r}]}{P[m_E]} \cdot e^{-j\frac{4\pi f_{Low}\Delta r}{c}}}_{D(\Delta r)e^{j\phi(\Delta r)}} \qquad (96)$$

where $D(\Delta r)$ is the magnitude component of the error factor and $e^{j\phi(\Delta r)}$ is the phase.

In theory, if the value of Δr can be accurately determined, we were able to recover the ideal range profile from the experimental range profile based on equation (96), such that the negative influences from the motion errors on the SAR images can be removed. However, in reality, the accurate value of Δr is difficult to compute, which means recovering the ideal range profile directly from the experimental one is not addressable.

Also, the autofocus algorithm mentioned in Chapter 3 above cannot solve the problems associated with the motion errors. When errors are taken into account, the basic signal model of the autofocus algorithm is shown in equation (34), which can be further expanded as:

$$\widetilde{\boldsymbol{Im}}_{\boldsymbol{k}} = \begin{bmatrix} Im_{k,1} \cdot e^{j\phi_k} \\ Im_{k,2} \cdot e^{j\phi_k} \\ \vdots \\ Im_{k,(N_x \times N_y)} \cdot e^{j\phi_k} \end{bmatrix}, k = 1,2,3, \dots, N_p \qquad (97)$$

where $Im_{k,i}$ represents the ideal image value of the i^{th} pixel from the k^{th} pulse and e^{ϕ_k} is the phase error associated with the k^{th} pulse. According to equation (97), there are two important characteristics of the basic signal model:

(1) The error applied to each pixel of the image corresponding to a specific pulse is purely phase error, with a constant magnitude of 1.

(2) All pixels of the image corresponding to a specific pulse have the same phase error.

The influence of the motion error on multiple pixels in the image is shown in Figure 19. Following equation (91), the relationship between r_I and r_E for Pixel 1 can be written as equation (98) and the relationship between r_I and r_E for Pixel 2 can be written as equation (99).

$$\Delta r_1 = r_{E_1} - r_{I_1} \tag{98}$$

$$\Delta r_2 = r_{E_2} - r_{I_2} \tag{99}$$

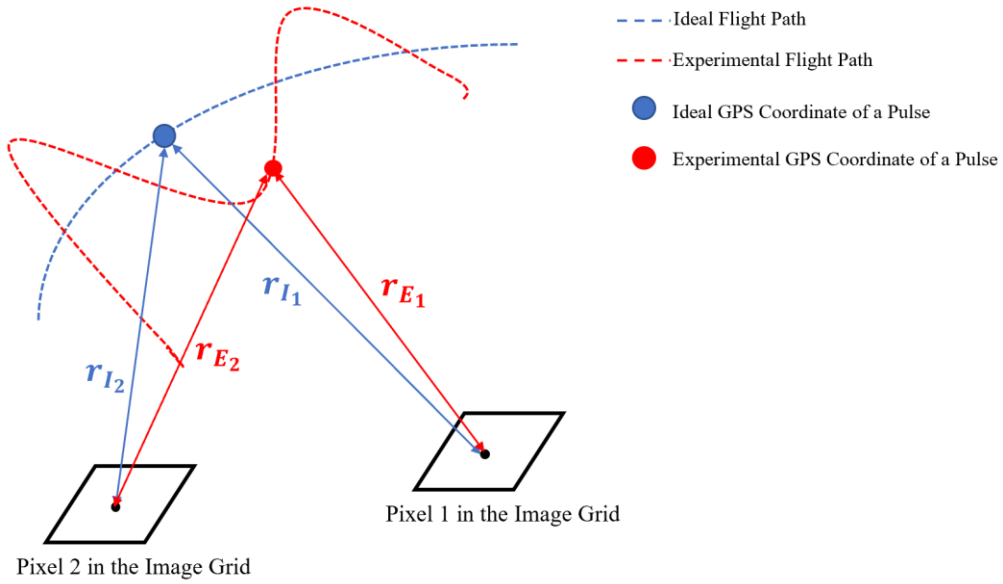

Figure 19: Influence of the Motion Error on Multiple Pixels

Δr_1 and Δr_2 from equations (99) and (100) are not necessarily equal to each other. This conclusion can also be applied to other pixels in the image grid. Based on equation (96), when the influences of the motion error to all the pixels in the image grid are taken into account, the relationship between the experimental pixel value and ideal pixel value the k^{th} pulse is:

$$\widetilde{\boldsymbol{Im}}_{\boldsymbol{k}} = \begin{bmatrix} Im_{k,1} \cdot \frac{1}{D(\Delta r_1)} \cdot e^{-j\phi(\Delta r_1)} \\ Im_{k,2} \cdot \frac{1}{D(\Delta r_2)} \cdot e^{-j\phi(\Delta r_2)} \\ \vdots \\ Im_{k,(N_x \times N_y)} \cdot \frac{1}{D(\Delta r_{(N_x \times N_y)})} \cdot e^{-j\phi(\Delta r_{(N_x \times N_y)})} \end{bmatrix}, \quad k = 1,2,3,\dots,N_p \tag{100}$$

where $Im_{k,i}$ represents the ideal image value of the i^{th} pixel from the k^{th} pulse; $\frac{1}{D(\Delta r_i)}$ is the magnitude error associated with the i^{th} pixel from the k^{th} pulse; $e^{-j\phi(\Delta r_i)}$ is the phase error associated with the i^{th} pixel from the k^{th} pulse. Since Δr_1, Δr_2, …, $\Delta r_{(N_x \times N_y)}$ in equation (100) are not necessarily equal to each other, the error factors $\frac{1}{D(\Delta r_i)} \cdot e^{-j\phi(\Delta r_i)}$ for different values of i are not necessarily equal to each other.

The comparison between equations (97) and (100) shows that equation (100) does not satisfy the two important characteristics from (97). In other words, the influences of the motion error to the SAR image violate the basic assumption of the proposed autofocus algorithm in Chapter 3 and therefore, the autofocus algorithm cannot solve the problems associated with the motion errors.

CHAPTER 6: Conclusion and Future Work

In this project, we implemented backprojection and autofocus algorithms in image processing software for a drone-SAR system. Based on radar and GPS data from a series of experiments, we demonstrated that the software could construct SAR images with high resolution. Although in general, experimental SAR images matched well with expectations, we observed the effect of errors on the SAR images. Additional tests of the drone-SAR system not only provided us with a further understanding of these errors, but also allowed us to correct some errors by calibrating parameters in the imaging software.

Based on the success from the team, there are two directions for future works. The first direction for future work is to improve the performance of 2-D image construction for the current drone-SAR system. Enhancements include: Kalman filtering [14] for fusion of GPS and accelerometer data for improved position accuracy; wi-fi control of data acquisition; improved calibration of chirp rate and signal delay; etc. The second direction for future work is to find new applications for the current drone-SAR system. Due to the capacity from SAR system to provide vision under situations when optical systems are not available, as well as the high-degree of flexibility brought by the drone platform, the drone-SAR system can be extensively applied to different fields, such as constructing 3-D SAR images, security monitoring, industry supervision, emergency response, navigation without GPS, interferometric SAR [15], etc.

CHAPTER 7: Reference

[1] A. W. Doerry and F. M. Dickey, "Synthetic aperture radar," *Optics and Photonics News*, vol. 15, no. 11, pp 28-33, 2014.

[2] D. Chen, T. Dean, B. Fair and L. Newton, “Light-weight SAR imaging system for UAS: ECE 4901 final report.” *SAR Quadcopter Project*, 2017. [Online]. Available: https://drive.google.com/drive/folders/0BzYlqaSHVRKNS3FUS2dHcHc1VDA. [Accessed: Feb. 10, 2018].

[3] B. Downs, A. Pycraft, and L. Smith, “Synthetic aperture radar on an unmanned aircraft system: ECE 4901 final report.” *SAR Quadcopter Project*, 2018. [Online]. Available: https://drive.google.com/drive/folders/1cN1RCiVxxn8ZJKRT9c_fLdZ4ks87_DV6. [Accessed: Oct. 4, 2018].

[4] Federal Aviation Administration, “FAA regulations,” *faa.gov*, Oct. 27, 2017. [Online]. Available: https://www.faa.gov/regulations_policies/faa_regulations/. [Accessed: Aug. 19, 2018].

[5] Federal Communications Commission. “Rules & regulations for title 47,” *fcc.gov*, Aug. 16, 2018. [Online]. Available: https://www.fcc.gov/wireless/bureau-divisions/technologies-systems-and-innovation-division/rules-regulations-title-47. [Accessed: Aug. 19, 2018].

[6] The Ohio State University. “Use of unmanned aircraft systems (UAS),” oaa.osu.edu, Apr. 2, 2018. [Online]. Available: https://oaa.osu.edu/sites/default/files/uploads/policies/UAS-Policy.pdf. [Accessed: Aug. 19, 2018].

[7] L.A. Gorham and L.J. Moore, “SAR image formation toolbox for MATLAB,” in *Proc. of SPIE Defense Security, and Sensing, 5-9 Apr. 2010, Orlando, Florida, United States* [Online]. Available: https://www.spiedigitallibrary.org/conference-proceedings-of-spie/7699/769906/SAR-image-formation-toolbox-for-MATLAB/10.1117/12.855375.full. [Accessed: Aug. 19, 2018].

[8] J. N. Ash, "An autofocus method for backprojection imagery in synthetic aperture radar," *IEEE Geoscience and Remote Sensing Letters*, vol. 9, no. 1, pp. 104-108, Jan. 2012.

[9] D.C. Munson, J.D O'Brien, and W.K Jenkins, "A tomographic formulation of spotlight-mode synthetic aperture radar," *Proceedings of the IEEE*, vol. 71, no. 8, pp. 917-925, Aug. 1983.

[10] The Mathworks Inc., “Inverse fast Fourier transform,” *MATLAB Documentation*, R2018a, 2018. [Online]. Available: https://www.mathworks.com/help/matlab/ref/ifft.html. [Accessed: Aug.19, 2018].

[11] J.C. Hart, “Distance to an ellipsoid,” in *Graphics Gem IV*, San Mateo, CA: Morgan Kaufmann, 1994.

[12] The Mathworks Inc., “Window function gateway,” *MATLAB Documentation*, R2018b, 2018. [Online]. Available: https://www.mathworks.com/help/signal/ref/window.html. [Accessed: Oct.19, 2018].

[13] The Mathworks Inc., “Blackman window,” *MATLAB Documentation*, R2018b, 2018. [Online]. Available: https://www.mathworks.com/help/signal/ref/blackman.html. [Accessed: Oct.19, 2018].

[14] R.G. Brown and P.Y. Hwang, *Introduction to Random Signals and Applied Kalman Filtering*, Vol.3. NY: Wiley, 1992.

[15] M.A. Richards, "A beginner's guide to interferometric SAR concepts and signal processing [AESS Tutorial IV]," *IEEE Aerospace and Electronic System Magazine*, vol. 22, no. 9, pp. 5-29, Oct. 2007

[16] W.G. Carrara, R.S. Goodman and R.M. Majewski, *Spotlight Synthetic Aperture Radar Signal Processing Algorithms*, Norwood, MA: Artech House, 1995.